Research Article

Cancer Immunology Research

Entinostat Converts Immune-Resistant Breast and Pancreatic Cancers into Checkpoint-Responsive Tumors by Reprogramming Tumor-Infiltrating MDSCs

Brian J. Christmas[1], Christine I. Rafie[1], Alexander C. Hopkins[1], Blake A. Scott[1], Hayley S. Ma[1], Kayla A. Cruz[1], Skylar Woolman[1], Todd D. Armstrong[1], Roisin M. Connolly[2], Nilo A. Azad[1,2], Elizabeth M. Jaffee[1,2], and Evanthia T. Roussos Torres[1,2]

Abstract

Immune-checkpoint inhibition (ICI) has revolutionized treatment in cancers that are naturally immunogenic by enabling infiltration of T cells into the tumor microenvironment (TME) and promoting cytotoxic signaling pathways. Tumors possessing complex immunosuppressive TMEs such as breast and pancreatic cancers present unique therapeutic obstacles as response rates to ICI remain low. Such tumors often recruit myeloid-derived suppressor cells (MDSCs), whose functioning prohibits both T-cell activation and infiltration. We attempted to sensitize these tumors to ICI using epigenetic modulation to target MDSC trafficking and function to foster a less immunosuppressive TME. We showed that combining a histone deacetylase inhibitor, entinostat (ENT), with anti–PD-1, anti–CTLA-4, or both significantly improved tumor-free survival in both the HER2/neu transgenic breast cancer and the Panc02 metastatic pancreatic cancer mouse models. Using flow cytometry, gene-expression profiling, and *ex vivo* functional assays, we characterized populations of tumor-infiltrating lymphocytes (TILs) and MDSCs, as well as their functional capabilities. We showed that addition of ENT to checkpoint inhibition led to significantly decreased suppression by granulocytic MDSCs in the TME of both tumor types. We also demonstrated an increase in activated granzyme-B–producing $CD8^+$ T effector cells in mice treated with combination therapy. Gene-expression profiling of both MDSCs and TILs identified significant changes in immune-related pathways. In summary, addition of ENT to ICI significantly altered infiltration and function of innate immune cells, allowing for a more robust adaptive immune response. These findings provide a rationale for combination therapy in patients with immune-resistant tumors, including breast and pancreatic cancers. *Cancer Immunol Res; 6(12); 1561–77. ©2018 AACR.*

Introduction

Immunotherapy has changed the standard of care for some patients with advanced cancers and has great promise to prevent recurrence and prolong survival due to the long-term memory capabilities of the adaptive immune system. Although the presence of tumor-infiltrating lymphocytes (TILs) and evidence of immune activation have been associated with improved outcomes in $HER2^+$ and triple-negative breast cancers (TNBCs; refs. 1, 2), only modest response rates have been observed with use of single-agent immune-checkpoint inhibitors (ICIs; refs. 3–10). Preclinical studies have focused on understanding these therapies in TNBC models (11) but have yet to thoroughly examine other subtypes of breast cancer. It has also been previously reported that antibodies blocking programmed cell death protein-1 (anti–PD-1) can significantly improve the activity of anti-HER2 therapies, but we have yet to understand if there is any added benefit of other ICIs (12). Similarly, single-agent ICIs have been shown to be ineffective in the clinical setting in metastatic pancreatic ductal adenocarcinomas (PDACs; refs. 13, 14). However, efficacy has been seen using combinatorial approaches in preclinical models. It has been shown that priming the tumor with a vaccine sensitizes PDAC to anti–PD-1 therapy by inducing the infiltration of cytotoxic $CD8^+$ T cells (15). In PDAC patients, a similar vaccine was reported to induce TILs (15). Improved efficacy of both anti–PD-1 and anti–CTLA-4 was achieved in murine models of PDAC by reprogramming immunosuppressive tumor-associated macrophages (TAMs; ref. 16). Taken together, these studies indicate the possibility to sensitize traditionally nonimmunogenic tumors to ICI therapy if TILs can be recruited and induced and/or immunosuppressive factors reduced within the tumor microenvironment (TME).

The natural resistance of breast and pancreatic tumors to single-agent ICI therapy is due to a lack of infiltrating T cells and an abundance of suppressive immune cells such as MDSCs. Specifically, granulocytic (G-MDSC) and monocytic MDSCs (M-MDSC) collectively inhibit T-cell function by depleting L-arginine through arginase-1 (Arg-1) expression and by inducing PD-L1 expression and the recruitment of regulatory T cells (Treg;

[1]Viragh Center for Pancreatic Clinical Research and Care, Bloomberg Kimmel Institute for Immunotherapy, Johns Hopkins University School of Medicine, Baltimore, Maryland. [2]Department of Oncology, and the Sidney Kimmel Cancer Center, Johns Hopkins University School of Medicine, Baltimore, Maryland.

Note: Supplementary data for this article are available at Cancer Immunology Research Online (http://cancerimmunolres.aacrjournals.org/).

Corresponding Author: Evanthia T. Roussos Torres, Johns Hopkins University, 1650 Orleans Street, CRB1 4M07, Baltimore, MD 21287. Phone: 310-729-0370; E-mail: ertorres@jhu.edu

doi: 10.1158/2326-6066.CIR-18-0070

refs. 16–19). High numbers of tumor-infiltrating myeloid cells correlate with early or local metastatic relapse (11). Previous studies have also shown changes in both circulating and tumor-infiltrating G-MDSCs in response to ICIs as a potential mechanism inhibiting antitumor responses (11, 20, 21). Thus, targeting and strategic reprogramming of these myeloid responses may overcome the immunosuppressive microenvironment and lead to an enhanced response to immune therapy through improved T-cell infiltration and function.

Studies using epigenetic modulatory drugs have shown promise in decreasing the infiltration and inhibitory capabilities of immunosuppressive cells. ENT ablates MDSC-mediated immunosuppressive activity when combined with ICIs in *in vivo* models of lung and renal cell cancer (21). Tomita and colleagues reported decreased circulating G-MDSCs and M-MDSCs in clinical samples of breast cancer patients treated with ENT in combination with an aromatase inhibitor compared with placebo combined with an aromatase inhibitor (22). Taken together, these data suggest that ENT can alter suppressive myeloid populations in multiple tumor types and synergize with immunotherapies to slow tumor growth and progression.

Our work explored the impact of ENT on the $HER2^+$ breast and PDAC TMEs in immunocompetent mice. Combination therapy of ENT + anti-PD-1 or ENT + anti-CTLA4 significantly improved survival as compared with mice treated with ENT alone, anti-PD-1 alone, or anti-CTLA-4 alone. ENT increased tumor infiltration by G-MDSCs and changed the polarity of their immunosuppressive ability to a nonfunctional phenotype. Flow cytometry and gene-expression profiling of treated tumors demonstrated altered expression of functional molecules and specific genetic pathways involved in proliferation and motility. Our observations suggest that G-MDSCs can exhibit multiple phenotypes, and support that a possible mechanism by which ENT allows ICIs to augment the infiltration and cytotoxicity of cancer-killing T cells is through the ablation of the immunosuppressive function of these infiltrating myeloid cells.

Materials and Methods

Mice and cell lines

All animal studies were approved by the Institutional Review Board of Johns Hopkins University. Animals were kept in pathogen-free conditions and were treated in accordance with institutional and American Association of Laboratory Animal Committee policies. The neu-N mice were originally from W. Muller McMaster University, Hamilton, Ontario, Canada. Colonies were renewed yearly from Jackson labs and bred in house by brother/sister mating. For studies of metastatic pancreatic cancer, we used male C57BL/6J (The Jackson Laboratories, stock #000664) mice. The T-cell receptor (TCR) transgenic mice are specific for the immunodominant HER2/neu epitope $neu_{420–429}$ and were made in house at the JHU Transgenic Core Laboratory as previously described (23). These mice were bred in house by brother/sister mating, and each animal was assessed for expression of the desired neu-specific Vβ region via staining with the $H\text{-}2D^q$ rat HER2/$neu_{420–429}$ PDSLRDLSVF tetramer (NIH Tetramer Core Facility).

All cell lines were regularly tested for *Mycoplasma* every 3 months in accordance with laboratory policy. NT2.5 cells were derived from spontaneous mammary tumors growing in female neu-N mice. *In vitro* cell lines were established and authenticated as previously described (24, 25). Culture conditions for NT2.5 cells were as follows: 37°C, 5% CO_2 in RPMI 1640 (Gibco, cat. 11875-093) supplemented with 20% fetal bovine serum (Gemini, cat. 100-106), 1.2% HEPES buffer (Gibco, cat. 15630-080), 1% L-glutamine (Gibco, cat. 25030-081), 1% MEM nonessential amino acids (Gibco, cat. 11140-050), 0.5% penicillin–streptomycin (Gibco, cat. 15140-122), 1% sodium pyruvate (Sigma, cat. S8636), 0.2% insulin (NovoLog, cat. U-100), and 0.02% gentamicin (Sigma, cat. G1397). Panc02 is a murine pancreatic tumor cell line with ductal morphology derived from a methylcholanthrenetreated C57B1/6 mouse and authenticated as previously described (26, 27). Culture conditions for Panc02 cells were as follows: 37°C, 10% CO_2 in DMEM (Gibco, cat. 11965-084) supplemented with 10% fetal bovine serum (Gemini, cat. 100-106), 1% L-glutamine (Gibco, cat. 25030-081), and 0.5% penicillin–streptomycin (Gibco, cat. 15140-122). $T2D^q$ cells are a fibroblast cell line established via transfection with murine $H\text{-}2D^q$ as previously described (28). Culture conditions for $T2D^q$ cells are as follows: 37°C, 5% CO_2 in RPMI supplemented with 10% fetal bovine serum (Gibco, cat. 100-106), 1% L-glutamine (Gibco, cat. 25030-081), 1% sodium pyruvate (Gibco, cat. 11965-084), 1% MEM nonessential amino acids (Gibco, cat. 11140-050), 0.5% penicillin–streptomycin (Gibco, cat. 15140-122), and 0.0007% Hygromycin B (Roche, cat. 10843555001). $T2D^q$ cells were cultured from frozen stocks and passaged three times before use.

Neu-N *in vivo* studies

The neu-N model is a syngeneic model where NT2.5 cells derived from a spontaneous mammary tumor were implanted via injection of 5×10^4 cells into the mammary fat pad of 7- to 8-week-old female neu-N mice (24). NT2.5 cells were cultured from frozen stocks and passaged twice before injection. Tumors were allowed to seed for 3 days prior to initiating treatment with various drug combinations as described below. Untreated mice developed palpable tumors within 1 week.

PDAC hemisplenectomy *in vivo* studies

To study metastatic PDAC, we used a hemisplenectomy model using 7- to 8-week-old syngeneic male C57BL/6J mice. This involved giving an intrasplenic injection of 2×10^6 of the pancreatic adenocarcinoma cell line (Panc02), as previously described (29–31). Panc02 cells were cultured from frozen stocks and passaged twice before injection. Metastases were allowed to establish for 7 days prior to starting treatment with various drug combinations as described below.

Rationale for mouse model selection

We selected the Panc02 hemisplenectomy model in order to recapitulate late-stage, metastatic disease, as this is most commonly how patients present. It should be noted that the Panc02 cell line was derived from a chemically induced tumor and contains a high mutational burden. Other groups circumvent this issue by using the genetically engineered KPC PDAC model, which results in pancreatic tumors that are more genetically and pathologically similar to human PDAC (30, 32, 33). Although the KPC model more accurately recapitulates primary disease in humans, these animals take a minimum 16 weeks to develop locally invasive PDAC and develop salivary tumors before metastases occur. These tumors grow large and often prohibit maintenance of mice long enough to study natural metastases (30). We recognize the shortcomings of using the Panc02 cell line, which is

why we paired the findings in this model with those in an extremely tolerant and nonimmunogenic breast cancer model (31). Future work with the KPC model could yield informative data to further translate the outcomes from preclinical models to human disease.

Drug dosing and selection

The ENT dosing solution (5 mg/kg) was made by suspending solid ENT (generously provided by Syndax Pharmaceuticals) in 0.5% methylcellulose via sonication and given by oral gavage daily for 3 weeks as described in Fig. 1A. To imitate oral gavage in control groups, 0.5% methylcellulose was given to vehicle mice, as well as mice receiving only antibody therapy, during the 3 weeks of ENT dosing. Mice received anti–PD-1 and/or anti–CTLA-4 twice a week for 3 weeks as stated in Fig. 1A. All studies in the neu-N model were performed with and without an anti-HER2 antibody to mimic treatment with and without trastuzumab. Anti-HER2 antibody was given once a week for 3 weeks as described in Fig. 1A. Following the initial 3 weeks of treatment maintenance dosing was continued with antibodies every other week. During maintenance therapy, animals receive 2 doses of anti–PD-1 and/or anti–CTLA-4 as well as one dose of anti-HER2 every other week as shown in Fig. 1A. Dosage of antibodies was as follows: anti–PD-1, 100 μg/mouse via intraperitoneal injection (i.p.); anti–CTLA-4, 100 μg/mouse i.p.; anti-HER2, 100 μg/mouse i.p. Monoclonal antibodies were obtained from Bio X Cell [anti–PD-1 (clone RPM1-14), anti–CTLA-4 (clone 9H-10), and anti-HER2 (clone 7.16.4)] and all were diluted to 0.5 mg/mL in PBS. Isotypes were used to treat vehicle mice and were also obtained from Bio X Cell [anti–PD-1 isotype: rat IgG2a (clone 2A3); anti–CTLA-4 isotype: polyclonal Syrian Hamster IgG; anti-HER2 isotype: mouse IgG2a (clone C1.18.4)]. All isotype antibodies were also diluted in PBS to 0.5 mg/mL. Dosages of each antibody were based off of prior studies (11). For mice receiving dual checkpoint antibody therapy, anti–CTLA-4 was given alone twice prior to addition of anti–PD-1, given that anti–CTLA-4 has been described as a T-cell repertoire–expanding agent, whereas anti–PD-1 has been determined to expand antigen-experienced T cells and help prevent the exhaustion of activated T cells (34).

For preliminary experiments using the demethylating agent SGI-110 (Astex) and the histone deacetylase inhibitor ACY-1215 (Acetylon), the PDAC hemisplenectomy model described above was used. Murine GVAX was prepared by irradiating a 1:1 mixture of Panc02 and the GM-CSF–secreting bystander line B78H1 as previously described (27, 35). A low dose of cyclophosphamide (100 mg/kg) was given 4 days after surgery, and GVAX was administered 5 days after surgery subcutaneously into 3 limbs of the mice. SGI-110 was administered subcutaneously into the flank of the animal at 24.4 mg/kg once a week over the course of 3 weeks while ACY-1215 was administered i.p. at 50 mg/kg daily. Following dosing of ACY-1215 and GVAX, survival was monitored until 120 days after surgery.

Rationale for use of entinostat

It has previously been shown that inhibition of class I HDACs targeted by ENT improves TLR signaling and cytokine production in myeloid cells (36), as well as cytokine signaling in T cells (37). Therefore, we hypothesized that use of ENT acted on these cell types to help sensitize nonimmunogenic tumors to ICIs. Although we showed that ENT did improve efficacy of ICIs in the neu-N and PDAC models, the mechanism appeared to be largely dependent on inhibiting the ability of MDSCs to produce immunosuppressive factors, specifically arginase-1 (Arg-1). Although a specific class I HDAC has not been identified as a regulator of Arg-1, a few studies illustrate a potential mechanism for the regulation of *Arg1* transcription involving HDAC2. It has previously been shown that a complex of Tet2 and HDAC2 is required for regulating the transcription of various inflammatory genes in macrophages, such as *Il6* and *Tnfα*, and this regulation can be abrogated with HDAC2 siRNA, as well as entinostat *in vitro* (38). Pan and colleagues showed that myeloid-specific knockout of Tet2 resulted in decreased Arg-1 expression in TAMs, as well as decreased ability to suppress T-cell proliferation (39). Taken together, these studies suggest Arg-1 could be regulated in a similar way to IL6, where Tet2 recruits HDAC2 to the arginase-1 promoter to regulate gene transcription. A rationale for addition of ICIs to ENT was also provided by two promising ongoing clinical trials that combine nivolumab, ipilimumab, and ENT (NCT02453620 and NCT03250273). However, mechanisms of action of these drug combinations remain elusive, and, thus, these preclinical studies were designed to inform rational design of clinical correlates for these trials and elucidate mechanisms behind potential antitumor responses.

Survival and tumor growth assays

Following injection of either Panc02 or NT2.5 cells, mice were treated for 3 weeks as depicted in Fig. 1A and then received maintenance therapy until succumbing to disease or requiring sacrifice due to tumor burden (up to 2 cm^3). In the neu-N model, mice were examined for palpable tumors starting 1 week after tumor cell challenge, and subsequently measured by calipers (±0.01 mm) twice weekly. Survival experiments were continued until mice were euthanized according to protocol due to tumor burden (neu-N model) or the development of ascites (PDAC model).

Tumor dissociation

To obtain single-cell suspensions from breast tumors, tumors were harvested, weighed, diced, and then dissociated using a tumor dissociation kit (Miltenyi Biotec, cat. 130-096-730) and the gentleMACS Octo Dissociator with heaters (Miltenyi Biotec, cat. 130-096-427) per the manufacturer's instructions. The 37C_m_TDK_2 program was used to dissociate tumors per the manufacturer's instructions. Samples were filtered using a 40-μm cell strainer, and red blood cells were lysed using ACK lysis buffer (Quality Biological, cat. 118-156-721). The resulting single-cell suspensions were used for subsequent isolation of specific immune cell types or flow cytometry as described below. Blood from neu-N mice was obtained via retro-orbital bleeds as per protocol. Red blood cells were lysed using ACK lysis buffer (Quality Biological, cat. 118-156-721). Isolated cells were analyzed via flow cytometry.

To obtain single-cell suspensions of livers containing metastases in the PDAC model, livers were harvested and processed by mashing the liver through 100-μm and 40-μm cell strainers as previously described (35). Red blood cells were lysed using ACK lysis buffer (Quality Biological, cat. 118-156-721), and liver pellets were resuspended in 40% Percoll (GE Healthcare Life Sciences, cat. 17-0891-01) and underlaid with 80% Percoll. The immune cell layer was then removed and analyzed via flow cytometry.

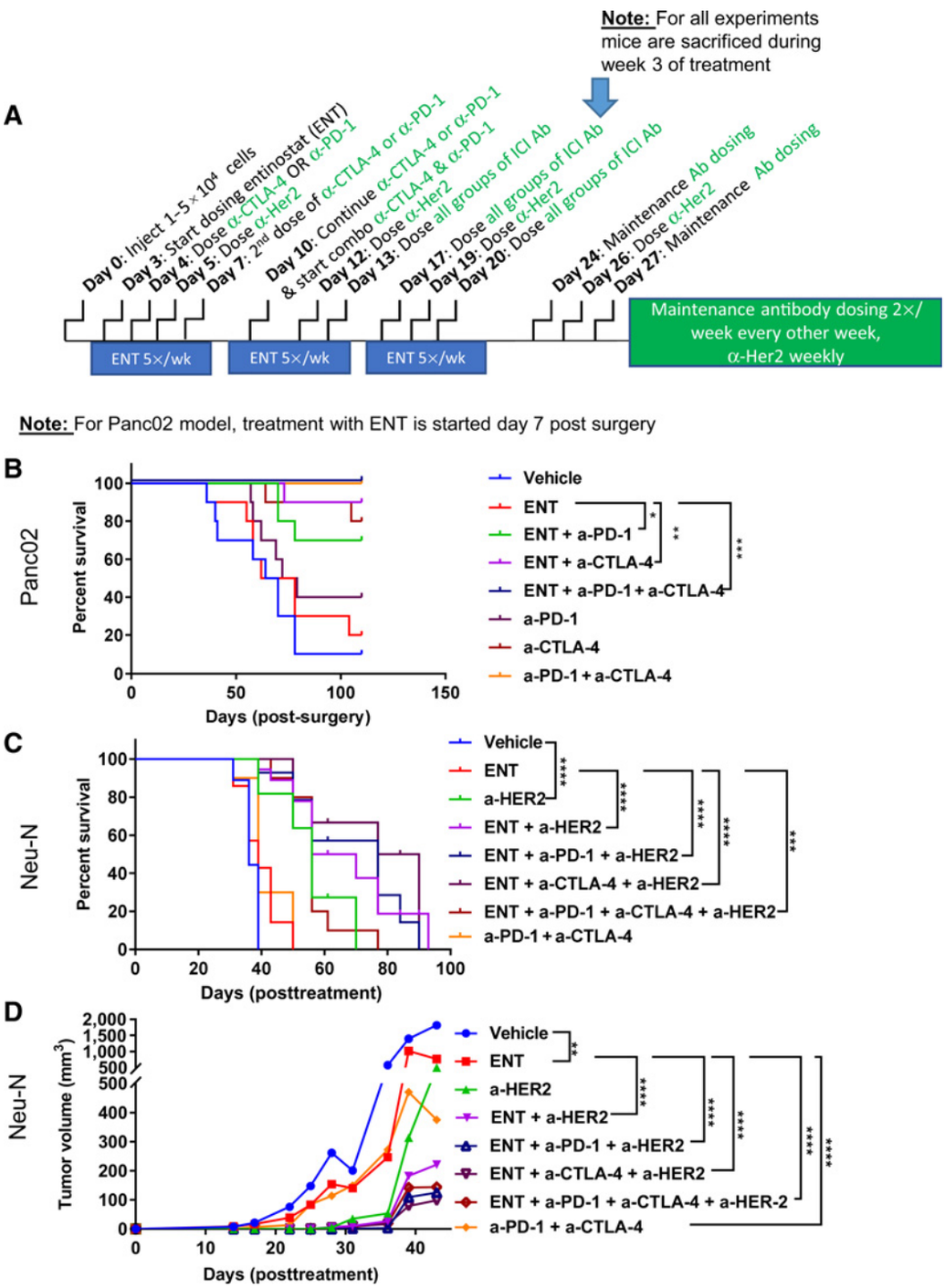

Figure 1.

Addition of entinostat to checkpoint inhibition significantly improves survival and slows tumor progression. **A,** Timeline of study design. In the neu-N model, ENT treatment was started 3 days following tumor implantation. For the metastatic pancreatic cancer model, ENT treatment began 7 days after hemisplenectomy and tumor implantation. In both models, ENT was given for 5 consecutive days each week over the course of 3 weeks. ICI antibody dosing was performed biweekly, whereas anti-HER2 was given weekly. For survival studies, mice continued to receive 2 doses of ICI antibody as well as 1 dose of anti-HER2 (neu-N model only) every other week after the first 3 weeks of treatment. Mice did not continue to receive ENT after the first 3 weeks of treatment. This was considered the maintenance phase of treatment. For all immune infiltrate analyses, mice were sacrificed during the third week of treatment. **B,** Survival of PDAC mice receiving ENT and ICIs. **C,** Survival and (**D**) tumor growth of neu-N mice receiving ENT and ICIs with anti-HER2. Statistics for tumor growth were calculated at day 43. For survival data, results were plotted using a Kaplan–Meier curve, and statistical significance was determined via a log-rank test; $n = 10$ mice/group. For tumor growth data, statistical significance was determined using a two-way ANOVA; $n = 10$ mice/group. All experiments were repeated at least 3 times. Statistically significant P values are shown as follows: *, $P < 0.05$; **, $P < 0.01$; ***, $P < 0.001$; ****, $P < 0.0001$.

Immune cell isolation

G-MDSCs were isolated from single-cell suspensions from tumors following tumor dissociation using Miltenyi Biotec's Myeloid-Derived Suppressor Cell Isolation Kit (cat. 130-094-538) according to the manufacturer's protocol. $Ly6G^+$ cells were positively selected to isolate G-MDSCs from $Ly6G^-$ M-MDSCs and were passed through LS columns (Miltenyi Biotec, cat. 130-042-401) twice to increase purity. M-MDSCs were isolated from the primary flow-through by subsequent Gr-1 antibody incubation and MS column isolation, as per manufacturer's instructions. Eluted G-MDSCs and M-MDSCs were then used for downstream assays described below.

$CD8^+$ neu-specific T cells were negatively isolated from spleens of the TCR transgenic mice described above by mashing spleens through 100-μm cell strainers. Red blood cells were lysed using ACK lysis buffer (Quality Biological, cat. 118-156-721), and $CD8^+$ T cells were isolated from spleen pellets using the EasySep Mouse $CD8^+$ Isolation Kit (StemCell, cat. 19853) per the manufacturer's instructions. $CD8^+$ T cells were then used for the *ex vivo* suppression assay described below.

Flow cytometry

Isolated single-cell suspensions were washed and then incubated for 30 minutes with Live/Dead Near-IR (Thermo Fisher, cat. L10119) according to the manufacturer's protocol, followed by a 30-minute incubation with the appropriate flow cytometry antibodies (Supplementary Table S1). For samples being analyzed for cytokine expression, single-cell suspensions obtained from tumor dissociations were plated at 37°C with anti-CD3/CD28 beads (Thermo Fisher, cat. 11453D) overnight at a bead-to-cell ratio of 1:1 per the manufacturer's instructions for T-cell activation. A protein transport inhibitor cocktail (eBioscience, cat. 00-4980-03) was introduced at 1× concentration during the last 4 to 6 hours of stimulation. The samples were harvested after 16 hours. For samples being stained for intracellular markers, cells were fixed and permeabilized (Transcription Factor Fixation/Permeabilization kit, eBioscience, cat. 00-5523-00) and then incubated with the appropriate antibodies for 30 minutes. Samples were run on a CytoFLEX or Gallios (Beckman Coulter) cytometer and analyzed using FlowJo (FlowJo LLC) or Kaluza (Beckman Coulter).

Flow cytometry gating strategies

G-MDSCs and M-MDSCs were identified by gating out debris from bulk tumor based on forward scatter and side scatter. Single cells were then gated by forward scatter-area and forward scatter-height. Dead cells were then gated out of the bulk tumor cell population. T cells and mature macrophages were gated out by selecting the CD3 and F4/80 double-negative population, respectively. $CD11b^+$ cells were then gated, and G-MDSCs and M-MDSCs were differentiated using Ly6G versus Ly6C. G-MDSCs were defined as $Ly6G^+Ly6C^{lo}$, and M-MDSCs were defined as $Ly6G^-Ly6C^+$. See Supplementary Fig. S1A.

Of note, we found that staining with CD45 in combination with more specific markers, such as CD3 and CD11b, did not further exclude nonimmune cell types from the final gated populations compared with single staining with CD3 or CD11b. For example, there were very few cells that were positive for CD3 or CD11b and negative for CD45. Given these findings, we did not use CD45 in our final FACS panels. See Supplementary Fig. S1B.

In order to characterize the $CD8^+$ T cells, debris was gated out of bulk tumor based on forward scatter and side scatter. Dead cells were then gated out of the bulk tumor population and lymphocytes were subsequently selected as $CD3^+$ and then gated by CD4 versus CD8. To determine the activation state of $CD8^+$ T cells, $CD8^+$ cells were then gated by CD44 versus CD62L, as well as CD8 versus granzyme-B. The exhaustion state of $CD8^+$ T cells was determined by gating $CD8^+$ cells by PD-1 versus Lag3. In order to characterize the $CD4^+$ T cells, debris was gated out of bulk tumor based on forward scatter and side scatter. Dead cells were then gated out of the bulk tumor population and lymphocytes were subsequently selected as $CD3^+$ and then selected as $CD4^+$. See Supplementary Fig. S2A.

Ex vivo suppression assay

Isolated G-MDSCs were cocultured with peptide-specific stimulated T cells and quantified for T-cell proliferation. G-MDSCs were isolated from tumors following tumor dissociation as described above. Eluted G-MDSCs were cocultured with 1×10^5 CSFE-labeled $CD8^+$ neu-specific T cells isolated from untreated neu-specific TCR transgenic mice (23) at varying ratios (1:1–1:8 MDSC:T cells). Prior to plating, T-$2D^q$ antigen-presenting cells (APC) were pulsed with 0.4 μg of either R-$neu_{420–429}$ or control peptide (NP) for 4 hours; both purchased from the Johns Hopkins University Synthesis and Sequencing facility at greater than 95% purity. The APCs were simultaneously added to the cocultured $CD8^+$ T cells and MDSCs at a ratio of 2:1 APCs:T cells, and plates were incubated at 37°C for a total of 48 hours. Cells were then harvested, stained with Live/Dead NIR (Thermo Fisher, cat. L10119), as well as CD8 and Thy1.2, and analyzed via flow-cytometric analysis as described above. Dilutions of initial CFSE were indications of T-cell divisions, where fewer divisions indicated greater suppressive G-MDSC activity. All antibodies used are listed in Supplementary Table S1.

Due to the small number of infiltrating M-MDSCs, we were unable to isolate sufficient numbers of these cells to perform a suppression assay. We attempted using fluorescence activated cell sorting as an alternative method of isolating M-MDSCs. However, the sorted M-MDSCs had poor viability, which had confounding effects on this assay.

Arginase assay

Arginase activity was measured colorimetrically *ex vivo* using Abcam's Arginase Activity Assay Kit (cat. ab180877). G-MDSCs were isolated from tumors and processed as described above and plated per manufacturer's instructions. In short, cells were lysed with kit's lysis buffer at 1×10^6/1 mL and plated carefully in varying dilutions (30k or 60k cells per well) in duplicate in a flat-bottom, low-retention plate to avoid bubble formation. Target samples were incubated for 20 minutes at 37°C with H_2O_2 substrate solution, while background wells were incubated with additional buffer. Standards were prepared per kit instructions, and the enzymatic reaction mixture was prepared and added to all wells. Raw absorbance values were immediately obtained over a 30-minute period using a plate reader (Molecular Devices SpectraMax M3) at OD = 570 nm at 37°C. Arginase Activity Units were then calculated from raw absorbance values. ΔOD [ΔOD = (OD2 − ODbg2) − (OD1 − ODbg1)] was used to obtain the nmol of H_2O_2 generated by arginase, extrapolated from a standard curve of known H_2O_2 concentrations. Arginase activity is calculated as $(B/\Delta T^*V)^*D$ in units/mL, where B is the amount of H_2O_2 from standard curve (nmol), V is the sample volume added into reaction well (μL), D is the sample dilution factor. One unit of arginase activity refers to the amount of arginase that will generate 1.0 nmol of H_2O_2 per minute at pH 8 at 37°C.

Gene-expression profiling

RNA was extracted from whole tumors or G-MDSCs isolated from tumors using the Qiagen RNeasy extraction kit (cat. 74104). Using a NanoDrop ND-1000, RNA quality and quantity were determined (samples with A260/280 < 1.8 were excluded). Gene expression was measured on the NanoString nCounter Analysis System (NanoString Technologies). The NanoString PanCancer Immune CodeSet (cat. XT-CSO-MIP1-12) was used to perform the nCounter Gene-Expression Assay for whole tumor samples, whereas the Mouse Myeloid Innate Immunity CodeSet (cat. XT-CSO-MII2-12) was used to perform nCounter Gene-Expression Assay for isolated G-MDSCs. Quantification of target mRNA in each sample was performed by detection within the nCounter Digital Analyzer. The data obtained from the PanCancer Immune CodeSet were deposited on the public database GEO under the accession number GSE121031. The data obtained from the Mouse Myeloid Innate Immunity CodeSet were deposited on the public database GEO under the accession number GSE121030.

Gene-expression analysis

Data from the NanoString nCounter system were normalized to the internal positive controls and housekeeping genes using the recommended settings in the nSolver software normalization module (NanoString Technologies). Normalized data were exported, and differential expression analysis was performed using a linear model method with the limma package (40) for the R programming language. To identify pathways that were differentially expressed in each treatment, the gage package (41) was used to test for differentially expressed KEGG pathways. Pathways of interest were visualized using the pathview package (42).

QC plots for NanoString cell typing

The QC plots show the correlation between genes included in the assay that are used to call specific cell types. nSolver uses expression data from *Lag3*, *Cd244*, *Eomes*, and *Ptger4* to call the "Exhausted CD8" set and expression data from *Cd6*, *Cd3d*, *Cd3e*, *Sh2d1a*, *Trat1*, and *Cd3g* to call the "T-cell" set. These plots report how well the expression of the genes within each cell type set correlate with each other. In our data from the PanCancer Immune panel, the algorithm to call cell types uses *Cd3g* and *Cd3d* for "T cells" and *Lag3* for "Exhausted CD8" cells. Due to the inherent variability between animals, more than the recommended 4 biological replicates are likely necessary to prevent the nSolver algorithm from discarding genes used to make cell type calls. See Supplementary Fig. S2B and S2C.

Quantitative PCR (qPCR)

Reverse transcription of mRNA and subsequent qPCR was performed on RNA isolates to validate expression changes seen in the NanoString analysis. RNA extracted from isolated G-MDSCs and whole tumor (Qiagen RNeasy kit, cat. 74104) were normalized to 10 ng/μL, and 1 μg of total RNA was used for reverse transcription. The SuperScript VILO cDNA Synthesis Kit (Invitrogen; #11754050) was used following the manufacturer's instructions. qPCR of subsequent cDNA was performed using gene-specific proprietary primer and probe constructs for selected genes obtained from TaqMan (Thermo Fisher, see individual product numbers per gene) and used with TaqMan Universal Master Mix II, no UNG (Applied Biosystems; #4440040) following the manufacturer's instructions. qPCR was performed on the StepOnePlus real-time PCR system (Applied Biosystems). To validate the ERBb pathway, *Tgfα* (Mm00446231_m1) and *Egf* (Mm004438696_m1) were checked; for the mTOR pathway, *Tgfα* (Mm00446231_m1) and *Frizzled4* (Mm00433382_m1) were checked; for the VEGF pathway, *Vegfa* (Mm01281449_m1) and *Cox2* (Mm03294838_g1) were checked. For the leukocyte transendothelial migration pathway, *Pik3cg* (Mm00445038_m1) and *Vcam1* (Mm01320970_m1) were checked; for the osteoclast differentiation pathway, *Infγ (*Mm01168134_m1) and *Il1b* (Mm00434228_m1) were checked. *18s* (Mm04277571_s1) was used as a control, and *Stat3* (Mm01219775_m1) and *Arg1* (Mm00475988_m1) were also checked. The two-step real-time PCR cycling conditions used were 95°C for 20 seconds, 40 cycles of 95°C for 3 seconds, and then 60°C for 30 seconds. Gene expression was quantified from raw data by calculating mean CT values from the 3 replicates and comparing the ΔCT values of each gene to the 18s reference gene. Fold changes were quantified as $2^{\Delta\Delta CT}$ and plotted against corresponding NanoString fold-change values.

Western blots

G-MDSCs were isolated from whole tumor of treated animals using Miltenyi Biotec's MDSC Isolation Kit and pooled by treatment group. Samples being used for phospho-STAT3 analysis were subsequently stimulated with IL6 (20 ng/μL) for 25 minutes. Samples were lysed in RIPA buffer with added 1 mmol/L DTT, 1 mmol/L PMSF, and 1:100 protease/phosphatase inhibitor cocktail (Cell Signaling Technology; #5872S) and quantified by BCA (Pierce; #23225). Protein (125 μg) was run in 4% to 12% Bis-Tris gels under denaturing conditions. The LiCor Odyssey developing and imaging system was used, and the following primary antibodies were diluted in Odyssey Blocking Buffer (TBS) plus 0.2% Tween 20 at specified concentrations: Abcam anti-interferon gamma rabbit (1:1,000), Abcam anti-VEGFA rabbit (1:1,000), Abcam anti-EGF (1:1,000), Cell Signaling TNFα Rabbit monoclonal antibody (mAb; 1:1,000), Cell Signaling PI3 Kinase p110γ Rabbit mAb (1:1,000), Cell Signaling Stat3 Rabbit mAb (1:2,000), and Cell Signaling Phospho-Stat3 (Tyr705) Rabbit mAb (1:2,000). Membranes were blocked with Odyssey Blocking Buffer (TBS) for 1 hour and then incubated with primary antibody solution overnight at 4°C with gentle shaking. Membranes were washed with 1× TBS-T and subsequently incubated with the following secondary antibodies: 680RD Donkey anti-Chicken IgG (1:10,000), 800CW Donkey anti-Rabbit IgG (1:10,000) in Odyssey Blocking Buffer (TBS) plus 0.2% Tween 20. Membranes were protected from light during incubation with secondary mixture for one hour at room temperature with gentle shaking. Membranes were subsequently washed with 1× TBS-T and imaged with the Odyssey imaging system. Images were analyzed using ImageJ.

Statistical analyses

For survival data, results were plotted using a Kaplan–Meier curve, and statistical significance was determined via a log-rank test (n = 10 mice/group). For tumor growth data, statistical significance was determined using a two-way analysis of variance (ANOVA; $n = 10$ mice/group). For all flow and functional assessments, mice were sacrificed during the third week of treatment. For dot plots, each dot represents one mouse and each bar represents mean ± SEM ($n = 3$–5 mice/group). Significance was determined by a one-way ANOVA with Tukey multiple comparisons

test. All experiments were repeated at least 3 times. All statistical analyses listed here were performed using GraphPad Prism v7.00. Statistically significant *P* values are shown as follows: *, $P < 0.05$; **, $P < 0.01$; ***, $P < 0.001$; ****, $P < 0.0001$.

Results

Baseline expression of immune checkpoints on bulk tumor and immune cells

Previous studies have examined the expression of PD-L1 as a predictor of response and showed varied correlation between protein expression and response (8, 43, 44). Thus, we evaluated changes in expression of PD-1, PD-L1, and CTLA-4 via flow cytometry in bulk tumors, as well as on intratumoral $CD8^+$ T cells, $CD4^+$ T cells, and MDSCs (cell types determined by gating strategies outlined in the Materials and Methods section) to determine if changes in expression following treatment with ENT alone validate a rationale for combining ICIs with ENT. We found no significant changes in expression of these checkpoint molecules on bulk tumor, as well as on intratumoral $CD8^+$ T cells, $CD4^+$ T cells, and MDSCs, with the exception of PD-1 expression on $CD8^+$ T cells, which showed an increase in expression (Supplementary Fig. S3A–S3D). Thus, we considered that increased expression of checkpoint molecules within the TME may not be predictive of response to ICIs in our models. However, various groups have previously shown synergy between HDAC inhibition and various immunotherapies, including checkpoint inhibition, which does provide a rationale for addition of these checkpoint inhibitors to ENT as completed in our study (11, 21, 36, 37, 45). Specifically, previous studies showed that in the 4T1 breast cancer model, 5-azacytidine plus ENT decreased infiltration of MDSCs into the tumor and concluded that it was ENT driving this effect (11). We also performed a comparison of the HDACis ENT and ACY-1215 as well as a demethylating agent (SGI-110) in the murine PDAC model. We determined only ENT significantly improved survival over other drugs (Supplementary Fig. S4A). Thus, we chose to move forward using ENT given its efficacy in both tumor models. We substituted anti–PD-1 for GVAX as our immunotherapy, which yielded the same survival benefit when combined with ENT (Fig. 1B; Supplementary Fig. S4A). Thus, moving forward, we used checkpoint inhibitors as our immunotherapy instead of GVAX.

ENT priming sensitizes tumors to checkpoint inhibition and improves survival

We hypothesized that ENT would sensitize naturally immune-resistant tumors, which often fail to recruit T cells into their TME, to ICIs. To test this hypothesis, we evaluated ENT given in combination with anti–PD-1, anti–CTLA-4, or a combination of the 3 drugs in neu-N/$HER2^+$ breast cancer and Panc02 metastatic PDAC models. A final dosing schedule is shown in Fig. 1A. In the PDAC model, ENT + anti–PD-1, ENT + anti–CTLA-4, ENT + both ICIs, and anti–PD-1 + anti–CTLA-4 significantly improved survival over treatment with vehicle or ENT alone (Fig. 1B). In the neu-N model, treatment with anti-HER2 significantly improves survival and inhibits tumor growth (Fig. 1C and D), consistent with studies showing efficacy in patients treated with HER-directed therapy (46). Combination ENT + anti–PD-1 + anti-HER2, ENT + anti–CTLA-4 + anti-HER2, or ENT + anti-HER2 + both ICIs significantly improved survival compared with vehicle or ENT alone in the neu-N breast tumor model (Fig. 1C). Combination immunotherapy alone did not improve survival when compared with vehicle or ENT (Fig. 1C). The combination of ENT + both ICIs in the absence of anti-HER2 significantly improved survival (Supplementary Fig. S4B). Future studies will focus on the specific contribution of anti-HER2 to these therapies. However, for the remainder of the experiments presented herein, addition of anti-HER2 served to prove that the results were similarly efficacious (with and without it) to better inform the use of ENT + ICIs in patients receiving ongoing anti-HER2 therapy. Combination therapies with ENT + single ICIs led to a significant decrease in tumor burden in the neu-N model, both with and without anti-HER2 (Fig. 1C; Supplementary Fig. S4C).

Combined therapy shifts the TME from an M-MDSC- to a G-MDSC-dominated milieu

Given the improved antitumor immune responses observed in the mouse tumors, we next asked if ENT + ICIs were affecting MDSCs, as previous studies demonstrate decreased recruitment of MDSCs into the TME following similar therapies (11). To evaluate changes in MDSC populations, breast tumors and PDAC liver metastases were harvested following a full course of treatment. Immune cells were isolated and characterized as G-MDSCs and M-MDSCs via flow cytometry (Fig. 2A; Supplementary Fig. S1A). Analysis showed that treatment with ENT in combination with anti–PD-1 or anti–CTLA-4 shifted the MDSC population to be dominated by the less immunosuppressive G-MDSCs (ref. 20; Fig. 2B and C). Single-agent treatment with ENT significantly increased G-MDSCs in PDAC hepatic metastases (Fig. 2C), resembling the increased trends observed in the periphery of tumor-bearing neu-N mice (Supplementary Fig. S5A and S5B). However, the addition of ICIs was required to observe significant G-MDSC induction in the primary breast tumors. The observed increase in G-MDSCs was not the result of a redistribution between the proportions of myeloid cells because treatment of mice with combination therapies significantly increased the absolute number of G-MDSCs adjusted to tumor or liver weight (Supplementary Fig. S5C and S5D). Treatment with ICIs alone did not alter MDSC infiltration into the TME compared with vehicle, and no significant difference in infiltration by M-MDSCs in either model was seen (Fig. 2D and E).

ENT alters G-MDSC function, rendering them less immunosuppressive

Because we observed increased recruitment of G-MDSCs into tumors of mice in the setting of decreased tumor burden, we evaluated the function of these cells. Traditionally, production of Arg-1 by MDSCs is used as a marker of their immunosuppressive capability (21). Thus, we performed immunosuppression assays and determined Arg-1 production both *ex vivo* and by flow cytometry. Data from immunosuppression assays revealed that the ability of G-MDSCs to suppress T-cell proliferation is inhibited in mice receiving ENT (Fig. 3A). Arg-1 protein expression was evaluated in both G-MDSCs and M-MDSCs using a colorimetric arginase activity assay in the neu-N model (Fig. 3B and C) and by flow cytometry in the neu-N and PDAC models (Supplementary Fig. S6A–S6D). Results from both assays indicated that G-MDSCs and M-MDSCs isolated from ENT + ICI–treated mice produced significantly less Arg-1. Taken together, these data suggest that the impaired immunosuppressive function of tumor-infiltrating G-MDSCs is, at least in part, due to decreased Arg-1 production.

Evaluation of PD-L1 was also investigated as a measure of MDSC-suppressive cell function. We analyzed the surface expression of PD-L1 on intratumoral G-MDSCs by flow cytometry. PD-L1 expression was significantly reduced on G-MDSCs with ENT + ICI treatment (Supplementary Fig. S6E and S6F). This suggested that treatment of G-MDSCs with ENT reduced their ability to inhibit T-cell activity by diminishing availability of the PD-L1/PD-1 T-cell inhibitory pathway.

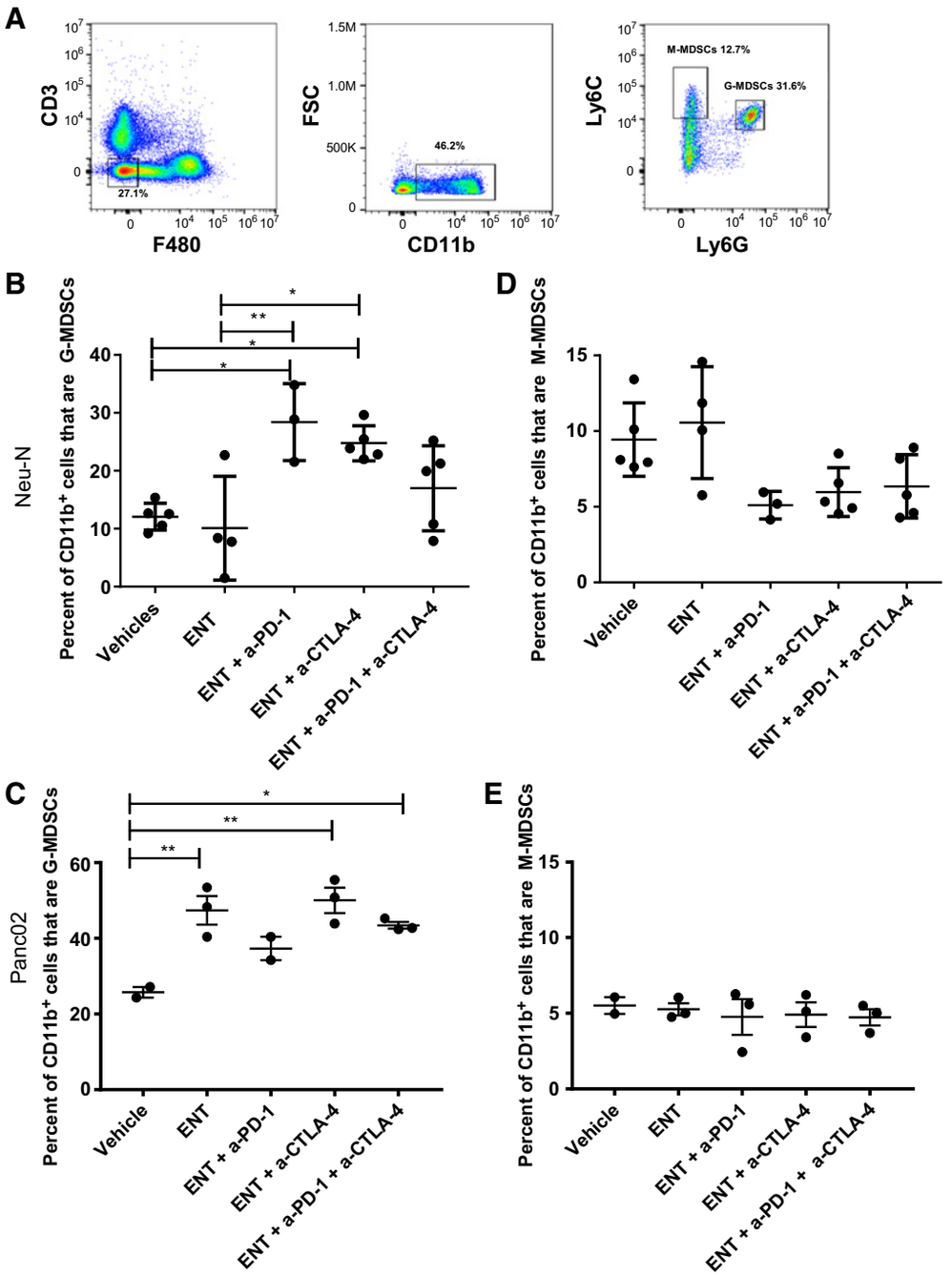

Figure 2.

ENT + ICI combination significantly increases infiltration of G-MDSCs into the TME. **A,** Gating strategy for identification of MDSCs by flow cytometry. G-MDSCs: $CD3^-F4/80^-CD11b^+Ly6G^+Ly6C^{lo}$; M-MDSCs: $CD3^-F4/80^-CD11b^+Ly6G^-Ly6C^+$. **B,** Changes in G-MDSC infiltration in breast tumors and (**C**) hepatic metastases of PDAC mice. **D,** Changes in M-MDSC infiltration occur in breast tumors of neu-N mice and (**E**) in hepatic metastases of PDAC mice. In all experiments, cells were isolated from breast tumors and livers containing PDAC metastases, respectively. For all flow data, mice were sacrificed during the third week of treatment. Each dot represents one mouse and each bar represents mean ± SEM; $n = 3$–5 mice/group. Significance was determined by a one-way ANOVA with Tukey multiple comparisons test. All experiments were repeated at least 3 times. Statistically significant P values are shown as follows: *, $P < 0.05$; **, $P < 0.01$.

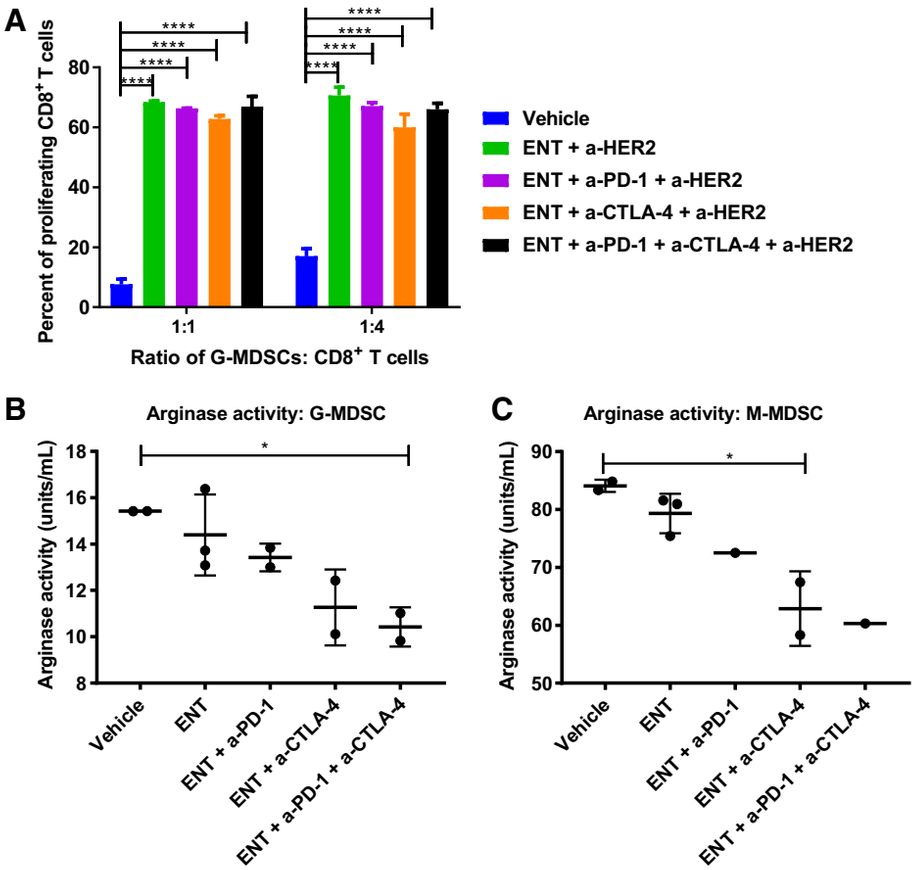

Figure 3.

ENT + ICI combination therapy inhibits immunosuppressive functions of MDSCs. **A,** Ly6G$^+$ G-MDSCs isolated from breast tumors of individual animals were cocultured with naïve neu-specific CD8$^+$ T cells and peptide-pulsed APCs. Proliferation was determined by CFSE staining. Each bar is an average of 3–4 mice/treatment group. Error bars indicate mean ± SEM. Significance was determined by a one-way ANOVA with Tukey multiple comparisons test. Changes in arginase activity of (**B**) G-MDSCs and (**C**) M-MDSCs isolated from treated breast tumors determined via colorimetric assay. For functional assays, mice were sacrificed during the third week of treatment. Each dot represents one mouse and each bar represents mean ± SEM (n = 3–5 mice/group). All experiments were repeated at least 3 times. Statistically significant P values are shown as follows: *, $P < 0.05$; ****, $P < 0.0001$.

ENT + ICI therapy significantly alters the signaling pathways involved in myeloid function

ENT alters the global acetylation state of cells (47), but its effect on subpopulations of myeloid cells has not been thoroughly studied. To identify possible mechanisms for their impaired function, we utilized NanoString transcript profiling to evaluate broad changes in the transcriptome of isolated G-MDSCs induced by treatment. Treatment with ENT and subsequently anti–CTLA-4 and/or anti–PD-1 significantly altered the expression of many genes important to G-MDSCs' function (Fig. 4A). Further evaluation revealed relevant pathways that were significantly upregulated or downregulated and contained significantly altered genes that drove the differential regulation of these pathways (Fig. 4B and C; Supplementary Fig. S7A and S7B). We narrowed our focus to certain pathways and genes that may be more specifically responsible for the observed MDSC phenotypes and only report treatment combinations that showed significant changes across all biological replicates (Fig. 4B and C). Our data reveal several observations. First, treatment with ENT alone and ENT + anti–PD-1 decreased expression of genes in both the ErbB and VEGF signaling pathways compared with vehicle-treated mice (Fig. 4B). However, expression was increased in both pathways in mice treated with ENT + anti–CTLA-4 (Fig. 4C). Second, treatment with ENT + anti–PD-1 downregulated the mTOR pathway (Fig. 4B), whereas ENT + anti–CTLA-4 increased overall expression of the pathway (Fig. 4C). Figure 4D depicts the VEGF pathway, highlighting key genes altered due to treatment with ENT compared with vehicle. Fourth, significant changes due to ENT + ICI treatment in pathways involving adhesion and motility suggested that treatment with ENT + ICI increased G-MDSC trafficking, which may explain the observed increased in infiltration of G-MDSCs (Supplementary Fig. S7A and S7B). Fifth, changes in pathways controlling different hormone production, apoptosis, and MAPK signaling were observed (Supplementary Fig. S7A and S7B). Finally, we found over 100 significantly differentially expressed genes independent of the aforementioned pathways. Key genes of interest are listed (Supplementary Fig. S7C). Expression of significantly altered pathways and genes of interest was validated using qPCR (Supplementary Fig. S8). We also validated these findings by investigating changes in protein expression via Western blot. EGF expression was analyzed to represent the ErbB pathway, VEGFA for the VEGF pathway, and TNFα for the mTOR pathway. Protein expression of STAT3, a key gene of interest, was evaluated along with activation of the STAT3 protein via phosphorylation at Tyr705. These data show that although the protein expression changes observed in G-MDSCs isolated from treated mice did not correlate with changes seen at the mRNA level (Supplementary Figs. S9A and S9B; S7C), a decrease in phospho-STAT3 was observed in treated mice (Supplementary Fig. S9A and S9B), indicating a decrease in STAT3 activity. Changes in protein expression of EGF, VEGFA, and TNFα correlated with mRNA expression in groups treated with ENT + anti–CTLA-4 compared with ENT-treated animals (Supplementary Fig. S9C). Changes in protein expression of EGF correlated with mRNA expression in groups treated with ENT compared with vehicle-treated animals (Supplementary Fig. S9D). However, changes in

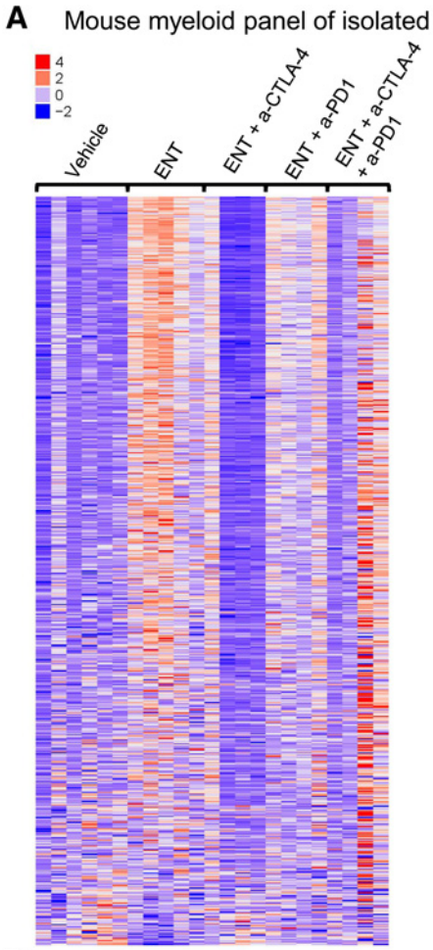

B Pathways downregulated

Treatment	KEGG pathway	*P*	Most differentially expressed genes
Vehicle vs. ENT	ErbB	0.00939	Raf1, Areg, p21, Egf, Hbegf
	VEGF	0.04022	Raf1, Hras, Nfat, Pkc, p38
Vehicle vs. ENT + a-PD-1	ErBB	0.05165	Raf1, Areg, p21, Egf, Hbegf
	VEGF	0.05165	Raf1, Hras, Nfat, Pkc, p38
	mTOR	0.05165	Raf1, Fzd4, Fzd6, Fzd9, Hras

C Pathways upregulated

Treatment	KEGG pathway	*P*	Most differentially expressed genes
ENT vs. ENT + a-CTLA-4	ErbB	0.00083	Raf1, Areg, p21, Egf, Hbegf
	VEGF	0.03325	Raf1, Hras, Nfat, Pkc, p38
	mTOR	0.01336	Raf1, Fzd4, Fzd6, Fzd9, Hras

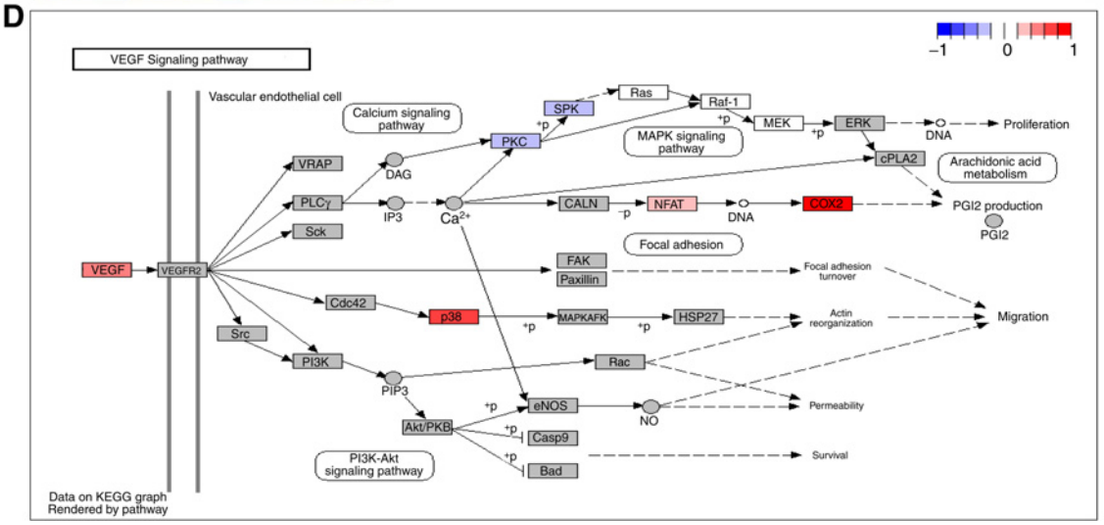

Figure 4.

HDACi + ICI combined therapy significantly alters the signaling pathway gene-expression profiles involved in myeloid function. **A,** Heat map of gene-expression changes in all-treatment groups compared with vehicle treatment alone. Red indicates upregulation; blue indicates downregulation. **B,** Tables listing selected significantly downregulated KEGG pathways and (**C**) significantly upregulated KEGG pathways, with the top 5 genes differentially regulated listed in the last column. **D,** Differentially regulated genes in the VEGF signaling pathway in mice treated with ENT versus vehicle. Expression of genes listed in white boxes was measured but did not show any fold change. Expression of genes in gray boxes was not measured. NanoString gene-expression profiling was performed once with at least 4 mice/group.

EGF protein expression did not correlate with mRNA expression in the ENT + anti–PD-1 group compared with vehicle-treated animals (Supplementary Figs. S7C and S9E). No correlation between changes in VEGFA protein expression and mRNA expression in either the ENT or ENT + anti–PD-1 groups was seen (Supplementary Fig. S9D and S9E), as well as for TNFα expression in the ENT + anti–PD-1 group (Supplementary Fig. S9E). Future work will focus on changes in expression of both genes and proteins within these pathways to determine if they play a mechanistic role in altered G-MDSC function.

ENT + ICIs promote infiltration of effector CD8$^+$ T cells independent of Treg infiltration

After determining that ENT + ICIs inhibited the immunosuppressive function of G-MDSCs, we sought to establish whether this change was sufficient to promote infiltration of functioning CD8$^+$ T cells into the TME (36). Cells were isolated from tumors, and changes within the T-cell populations were evaluated using flow cytometry. We observed increased infiltration of CD8$^+$ T effector cells and decreased naïve and memory CD8$^+$ T cells when ENT was combined with anti–PD-1, anti–CTLA-4, or both (Fig. 5A and B). Evaluation of the proliferative capacity of infiltrating CD8$^+$ T cells within the PDAC TME showed increased proliferation with the addition of ICIs, determined by Ki67 staining (Supplementary Fig. S10A). PDAC mice treated with ENT + anti–CTLA-4 also showed a significant increase in granzyme-B–producing CD8$^+$ T cells. A pattern suggesting an increase in granzyme-B–producing CD8$^+$ T cells was also observed in the anti-HER2 + ENT + anti–CTLA-4–treated neu-N mice. The addition of anti–PD-1 reduced this effect in both tumor types (Fig. 5C and D). IFNγ production by CD8$^+$ T cells was also measured. However, combination-treated mice only showed a trending increase in both models (Supplementary Fig. S10B and S10C). These data indicate that the combination of ENT with ICIs induced infiltration of effector CD8$^+$ T cells with cytotoxic capabilities.

Although the CD8$^+$ T cells appeared to exhibit improved antitumor activity, we wanted to characterize the ability of treatment to promote T-cell activation versus exhaustion. We evaluated the expression of various surface markers in CD8$^+$ T cells from tumors in both models, and first observed significantly increased expression of PD-1 (Supplementary Fig. S11A and S11B). Because PD-1 can be a sign of activation as well as exhaustion, we evaluated the coexpression of a second marker, Lag3. Coexpression of these molecules is indicative of exhausted CD8$^+$ T cells, whereas the absence of Lag3 on PD-1$^+$ CD8$^+$ T cells is indicative of activated T cells (48, 49). Our results only showed a significant increase in PD-1$^+$Lag3$^-$CD8$^+$ tumor infiltrating T cells from both models (Fig. 5E and F). We noted a pattern of nonsignificant increases of exhausted PD-1$^+$Lag3$^+$CD8$^+$ T cells (Supplementary Fig. S11C and S11D). These data support that most CD8$^+$ tumor infiltrating T cells in response to ENT + ICIs were activated and not exhausted. We also checked the coexpression of Tim3 and CTLA-4 with PD-1 as additional markers of exhaustion (48, 49) and found similar trends. Analysis of transcription factor expression revealed a 50% increase in terminally exhausted CD8$^+$ T cells in mice treated with ENT + anti–PD-1 + anti-CTLA-4 in both neu-N tumors and PDAC metastases (Supplementary Fig. S11E and S11F). These are also the treatment groups with the highest proliferative capacity. This analysis showed no significant change in progenitor exhausted CD8$^+$ T cells in the neu-N model and a 35% to 60% increase in the PDAC model (Supplementary Fig. S11G and S11H). Taken together, these data support that treatment generally induces an activated T-cell state.

Previous studies revealed that ENT + IL2 induces a decrease in tumor burden, which correlates with an increase in effector T cells and a reduction in tumor-infiltrating Tregs (33). Because Tregs have also been described as a major immunosuppressive component of the TME (50), we used flow cytometry to determine if ENT altered Treg infiltration. However, we only observed a trending decrease in Tregs in both models (Fig. 6A and B), which was not statistically significant.

ENT + ICIs significantly alter gene-expression profiles in immune signaling pathways

Our data showed that ENT broadly affected multiple populations of immune cells within the TME. Thus, we performed general immune transcriptome profiling on whole tumors isolated from the neu-N model using a PanCancer Immune-profiling gene panel for the NanoString platform. Numerous significant changes were found in multiple genes and pathways (Fig. 7A). Specifically, two pathways were found to be significantly altered (listed in the table in Fig. 7B). We report only treatment combinations that showed significant changes. One of these pathways, leukocyte transendothelial migration, was upregulated, suggesting a mechanism by which leukocytes may be able to traffic into the TME and contribute to an antitumor response in mice treated with ENT + anti–CTLA-4 (Fig. 7B). The osteoclast differentiation pathway was significantly upregulated in tumors from mice treated with ENT + anti–CTLA-4 versus ENT alone (Fig. 7B). Many of the genes involved in this pathway were also involved in pathways that contribute to the regulation of adaptive immunity. Our experiments also identified 20 individual genes significantly altered in cells from whole tumors treated with ENT + anti–CTLA-4 and ENT + anti–CTLA-4 + anti–PD-1 (Supplementary Table S2). Detailed investigation of these genes is necessary to determine how other immune compartments are being affected. Use of NanoString enables evaluation of immune cell subsets and related pathways. However, none of the immune cell subsets were significantly altered in this evaluation. Figure 7C demonstrates an increase in gene-expression profiles that suggest both "T cells" (determined by expression of *Cd3g* and *Cd3d*) and "exhausted CD8" (determined by expression of *Lag3*) showed a trending increase in treated groups, corroborating findings from flow cytometry (Fig. 5). QC plots depicting the correlations of the genes used to call these cell types are included in Supplementary Fig. S2B and S2C. Platforms for more directed approaches to investigation of gene-expression profiling are still evolving and can be limited in feasibility by large cohort animal studies, as seen with our findings using the NanoString platform. Future studies will evaluate gene expression at the single-cell level to work around the inherent biological variability associated with animal studies.

Discussion

We demonstrated in the neu-N and PDAC models that mice treated with the combination of ENT + ICIs exhibited significantly improved survival compared with mice treated with either ENT or ICIs alone. We also showed that the efficacy of ENT + anti–CTLA-4 treatment was associated with a significant increase in tumor-

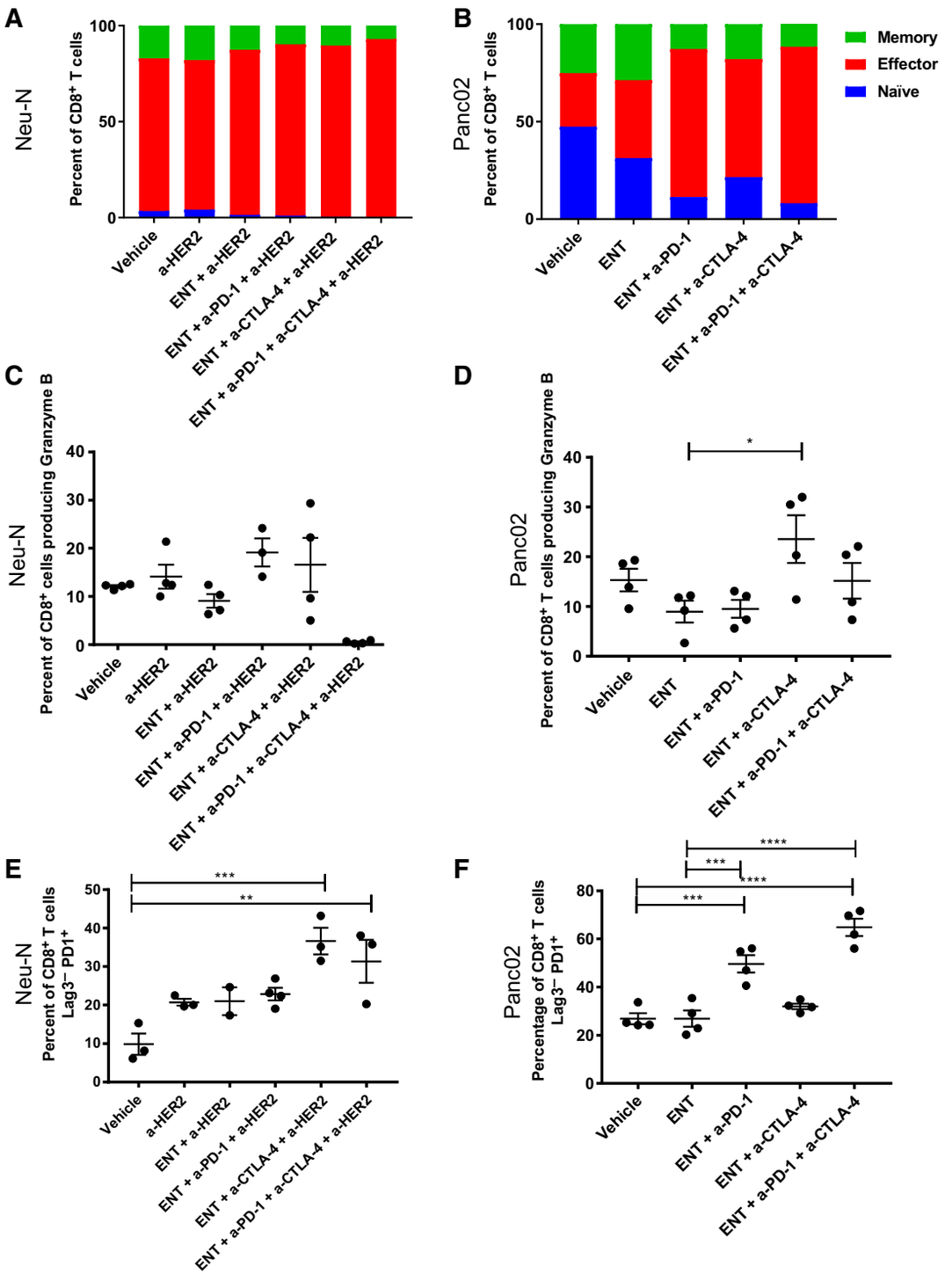

Figure 5.

HDACi + ICI combination therapy promotes infiltration of activated cytotoxic CD8$^+$ effector T cells. The proportion of infiltrating CD8$^+$ naïve (CD62L$^+$CD44$^-$), effector (CD62L$^-$CD44$^+$), and memory (CD62L$^+$CD44$^+$) T cells was evaluated. **A,** The percentage of infiltrating CD8$^+$ effector T cells in breast tumors and (**B**) PDAC hepatic metastases of treated mice. **C–F,** Cells were isolated from breast tumors and livers containing PDAC metastases, respectively. **C,** Change in infiltration of CD8$^+$ granzyme B$^+$ T cells in breast tumors and (**D**) PDAC hepatic metastases of mice receiving combined therapy. **E,** Exhaustion state of infiltrating CD8$^+$ T cells determined by coexpression of PD-1 and Lag3 in both the neu-N and (**F**) the PDAC model. For all flow data, mice were sacrificed during the third week of treatment. Each dot represents one mouse and each bar represents mean ± SEM (n = 3–5 mice/group). Significance was determined by a one-way ANOVA with Tukey multiple comparisons test. All experiments were repeated at least 3 times. Statistically significant P values are shown as follows: *, $P < 0.05$; **, $P < 0.01$; ***, $P < 0.001$; ****, $P < 0.0001$.

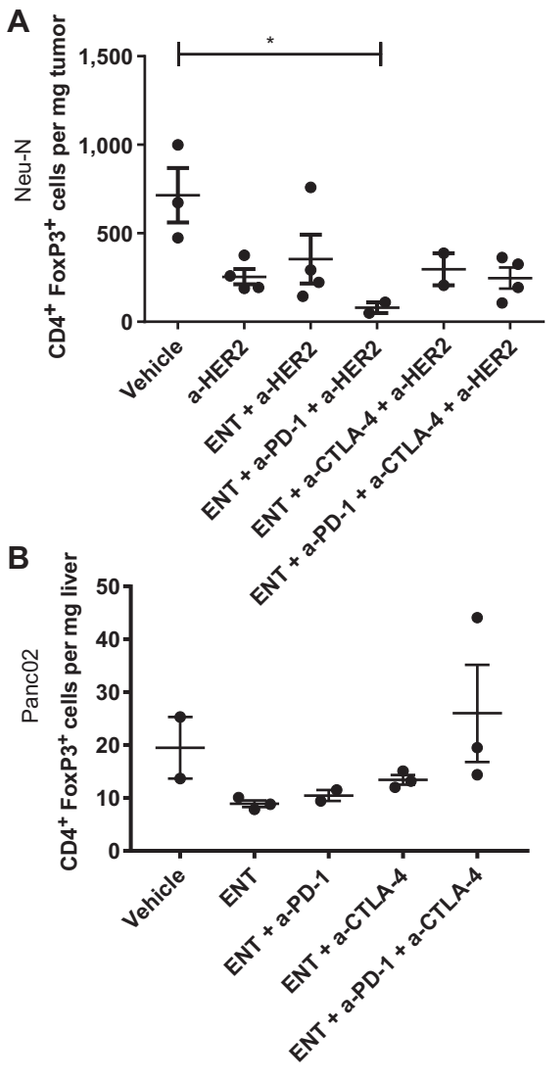

Figure 6.

HDACi + ICI combination therapy does not significantly alter Treg infiltration. Changes in Treg infiltration in breast tumors of (**A**) neu-N mice and (**B**) hepatic metastases of PDAC mice receiving therapy. Cells were isolated from breast tumors and livers containing PDAC metastases, respectively. For all flow data, mice were sacrificed during the third week of treatment. Each dot represents one mouse, and each bar represents mean ± SEM ($n = 3$–5 mice/group). Significance was determined by a one-way ANOVA with Tukey multiple comparisons test. All experiments were repeated at least 3 times. Statistically significant P values are shown as follows: *, $P < 0.05$.

infiltrating G-MDSCs that exhibited impaired immunosuppressive function. We also identified changes in important signaling pathways that converged to control and regulate myeloid immunosuppressive activities, which suggest novel mechanisms responsible for the observed MDSC dysfunction in tumors. ENT was primarily responsible for significantly affecting genes controlling myeloid function, such as those within the VEGF and ErbB pathways, and may have also acted to prime $CD8^+$ T cells by increasing their expression of PD-1, although the addition of anti–PD-1 further augmented these changes, resulting in altered signaling in the mTOR pathway. The combination of ENT + anti–CTLA-4 induced changes in expression of downstream signaling molecules, at which the three pathways converged, leading to a similar outcome on myeloid suppression. These data showed that it was the addition of ICIs to ENT that led to improved infiltration of activated $CD8^+$ T effector cells and increased cytotoxic characteristics. Examination of gene-expression changes in whole tumors revealed that addition of anti–PD-1 and/or anti–CTLA-4 affected T-cell trafficking. Taken together, these data elucidate a suggested mechanism by which ENT alters the function of myeloid cells and the addition of ICIs to ENT further alters the myeloid compartment and improves T-cell responses. This mechanistic understanding delineates the important effects of each individual drug on specific immune compartments within the TME. These data could be used for developing scientifically driven combinations of epigenetic- and immune-based therapies.

Various studies have shown that ENT can reduce tumor burden and alter MDSC infiltration, facilitating increased efficacy of single-agent ICIs in other murine models of cancer (11, 21, 36, 37, 45). These data support the therapeutic strategy of using agents that target multiple immune compartments within the TME, where ENT inhibits the immunosuppressive myeloid populations and ICIs allow for the activation and recruitment of T cells in order to induce a robust antitumor response. We showed that whereas ENT + anti–PD-1 + anti–CTLA-4 was efficacious, it did not significantly improve survival over ENT + anti–PD-1 or ENT + anti–CTLA-4. A previously proposed mechanism for improved survival is that addition of ENT to anti–PD-1 leads to decreased immunosuppressive capacity of tumor-infiltrating MDSCs and allows for increased infiltration of cytotoxic T cells (21). We not only confirmed these findings in breast and PDAC models but also expanded upon them by showing a decrease in Arg-1 protein activity and production (21). Given that our data were generated entirely *ex vivo*, it supports changes in Arg-1 protein production as a significant mechanism underlying the MDSC impairment reported. In further support of this proposed mechanism, our gene-expression profiling of isolated G-MDSCs allowed us to identify changes specific to the G-MDSC transcriptome in key signaling pathways such as VEGF, mTOR, and ErbB. Changes in Arg-1 and PD-L1 protein expression have not been analyzed in human MDSCs treated with ENT. However, a clinical trial has analyzed changes in MDSC populations as well as changes in CD40. CD40 has previously been described to be necessary in human MDSC-mediated T-cell suppression (51). Tomita and colleagues show that treatment of breast cancer patients with ENT significantly decreases CD40 expression (22), suggesting ENT may also induce immunosuppressive dysfunction in human MDSCs.

The most impactful finding of our work is the identification of changes in gene-expression responsible for the impaired immunosuppressive functions of G-MDSCs that are driven by ENT. First, we observed downregulation of genes within the VEGF signaling pathway in isolated G-MDSCs in ENT or ENT + anti–PD-1–treated versus vehicle-treated mice. Previous studies showed that elimination of VEGF can abrogate Arg-1 protein expression in intratumoral MDSCs and subsequently their ability to suppress T-cell proliferation (52), highlighting the importance of VEGF signaling in immunosuppressive functions of MDSCs. Second, decreased expression of genes in the ErbB signaling pathway was seen in isolated G-MDSCs with ENT or ENT + anti–PD-1 treatment. This may also contribute to the decrease

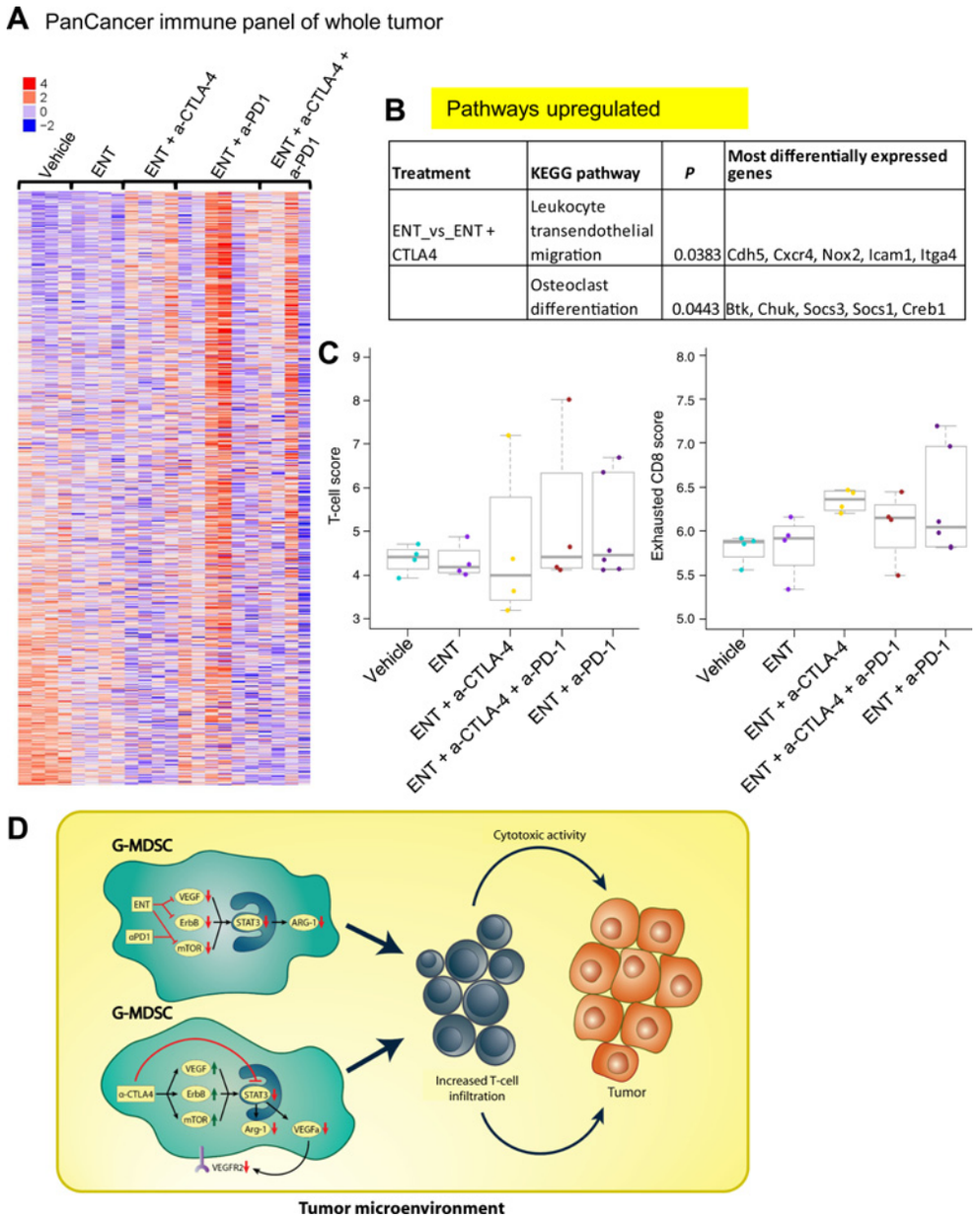

Treatment	KEGG pathway	P	Most differentially expressed genes
ENT_vs_ENT + CTLA4	Leukocyte transendothelial migration	0.0383	Cdh5, Cxcr4, Nox2, Icam1, Itga4
	Osteoclast differentiation	0.0443	Btk, Chuk, Socs3, Socs1, Creb1

Figure 7.

HDACi + ICI combination therapy significantly alters the leukocyte transendothelial migration pathway. **A,** Heat map of gene-expression changes comparing all-treatment groups using the PanCancer Immune-profiling gene set. Red indicates upregulation; blue indicates downregulation. **B,** Table of significantly altered KEGG pathways. Five most differentially expressed genes are listed in the last column. **C,** Graphs depicting an increase in genes indicative of bulk T cells and exhausted T cells in combination-treated groups. Genes upregulated are listed in red, and genes downregulated are in blue. Expression of genes listed in white boxes was measured but did not show any fold change. Expression of genes in gray boxes was not measured by the assay. **D,** Diagram showing proposed mechanism regulating decreased suppressive function of myeloid cells and increased infiltration of T cells as a result of treatment with ENT, anti–PD-1, and anti–CTLA-4. NanoString gene-expression profiling was performed once with at least 4 mice/group.

in suppressive nature of these cells because EGFR-deficient macrophages are known to produce less immunosuppressive factors, including Arg-1 (53). Taken together, ENT appears to be the treatment driving these observed changes, indicating that it may be inducing MDSC dysfunction by decreasing signaling within both pathways (Fig. 7D). Third, treatment with ENT + anti–PD-1 significantly decreased expression of genes within the mTOR pathway. It has previously been shown that inhibition of mTORC1 can disrupt the immunosuppressive abilities of myeloid cells, including Arg-1 protein expression (54, 55). Therefore, it is likely that PD-1 inhibition also contributes to the observed MDSC dysfunction through decreased mTOR signaling (Fig. 7D). We

evaluated protein expression of representative proteins for each pathway in order to attempt to validate the observed changes in gene expression of each pathway. Although some of these observed gene-expression changes correlated with similar changes in protein expression, others did not. This was expected given that posttranscriptional modifications often cause discrepancies between levels of message and protein. The reported changes in overall pathways were not determined by changes in expression of single genes, rather by the cumulative change of all genes in the pathway. Thus, expression of individual genes within a pathway was not representative of the overall reported pathway changes. Key genes directly affecting MDSC function will need to be identified before further protein analysis is pursued.

Gene expression within the mTOR, ErbB, and VEGF pathways was upregulated with ENT + anti–CTLA-4 treatment, although this treatment also inhibited MDSC function similar to the combination of ENT + anti–PD-1. We hypothesize that these differential gene-expression changes across treatment groups may converge at the transcription factor *Stat3*, which is downstream of all of the pathways we have mentioned (53, 56). STAT3 is known to be essential in MDSC immunosuppressive function (57) and has previously been shown to be specifically targeted by ENT in MDSCs in *in vitro* systems (21, 58–60). G-MDSCs from mice treated with ENT + anti–CTLA-4 showed a significant decrease in *Stat3* expression, whereas significant downregulation in upstream activators was observed in the ENT or ENT + anti–PD-1–treated groups. This suggests that the ultimate change in regulation of *Stat3* occurs either directly or indirectly depending on ICI treatment but leads to the same effect on G-MDSC function. The ENT + anti–CTLA-4–treated mice also exhibited a significant decrease in the expression of *Vegfa*, which has been shown to be a target of STAT3 transcriptional activity (61–63). Despite the increase in signaling intermediates in this pathway, a decrease in *Vegfa* expression, and subsequent VEGFR2 signaling, could be caused by less STAT3 activity. This could help explain the observed MDSC dysfunction with ENT + anti–CTLA-4, as inhibition of VEGFA signaling can prevent Arg-1 production (Fig. 7D; ref. 52). G-MDSCs from ENT + anti–CTLA-4–treated mice did show lower expression of *Arg1* compared with the mice receiving ENT + anti–PD-1, further indicating that inhibition of STAT3 signaling may be one of the driving mechanisms in the observed MDSC dysfunction. Taken together, we hypothesize that the mTOR, ErbB, and VEGF signaling pathways converge at *Stat3* to drive immunosuppressive functions of MDSCs. This hypothesis requires significantly more investigation, but given previous studies linking treatment with ENT to STAT3 activity (21) and linking STAT3 to the suppressive function of Arg-1 (57), this seems like a plausible explanation for our observations. Analysis of protein expression of STAT3 from neu-N mouse tumors did not follow the same trends as those observed at the mRNA level. However, investigation of phospho-STAT3 in isolated G-MDSCs showed a decrease in STAT3 phosphorylation in all-treatment groups compared with vehicle, indicating decreased STAT3 activity may play a role in the observed MDSC dysfunction in treated animals. It has been shown that HDAC2 is important in the regulation of inflammatory genes in myeloid cells (39), suggesting class I HDACs may play a role in the regulation of Arg-1 (38). Lastly, it should be noted that preliminary work using the HDAC6 inhibitor ACY-1215 did not improve survival when combined with immunotherapy, suggesting class II HDACs may not play a pivotal role in the functional capabilities of MDSCs. This is an area where future studies can aim to delineate the roles of class I and II HDACs in MDSC function as well as *Stat3* regulation.

Whereas modulation of MDSC function seemed primarily responsible for the improved survival observed with ENT + ICIs in these models, the addition of ICIs also significantly improved the infiltration and cytotoxic ability of $CD8^+$ T effector cells within the TME. We identified significant upregulation of the leukocyte transendothelial migration pathway, which likely aids in the infiltration of TILs, and the addition of anti–CTLA-4 to ENT drives this observed change. The 20 genes that were found to be significantly affected by treatment with ENT + anti–CTLA-4 seemed to be expressed in a wide range of immune cell types. This suggests that other cell types, such as dendritic cells and natural killer cells, may also be secondarily affected by ICIs but are not primarily responsible for improved survival in response to treatments in these tumor models. The observed increase in infiltration of activated T cells may also be explained by the induction of expression of immunogenic noncoding long terminal repeats (LTR) in tumor cells. A study by Brocks and colleagues showed that treatment with both a DMNTi and an HDACi leads to activation of these LTR elements (64). In the future, we will examine whether treatment with ENT without DNMTi can induce a biologically relevant amount of LTR expression *in vivo*.

In summary, these data support the use of ENT as a method of sensitizing nonimmunogenic tumors to ICI therapy. ENT primed the MDSC compartment of the TME to permit T-cell infiltration into tumors, thereby making them available for activation by ICI therapy. ICI therapy may also contribute to reprogramming MDSCs in favor of T-cell activity. These data have provided a deeper understanding of how to improve response to ICIs in patients with breast and pancreatic cancers. Specifically, they are informing the laboratory correlates for our clinical trials evaluating ENT + combined ICIs in advanced solid tumors with a dose expansion in advanced breast cancer (NCT02453620), as well as ENT + nivolumab in patients with unresectable PDAC (NCT03250273). The preclinical work presented here will provide the necessary scientific evidence to create rational combinations of immune therapies in future clinical trials to maximize efficacy of these promising treatments.

Disclosure of Potential Conflicts of Interest

E.M. Jaffee reports receiving commercial research funding from Bristol-Myers Squibb, Aduro Biotech, and Amgen; has ownership interest in Aduro Biotech; and is a consultant/advisory board member for Genocea, DragonFly, and Adaptive Biotech. No potential conflicts of interest were disclosed by the other authors.

Authors' Contributions

Conception and design: B.J. Christmas, R.M. Connolly, N.A. Azad, E.M. Jaffee, E.T. Roussos Torres

Development of methodology: B.J. Christmas, B.A. Scott, H.S. Ma, T.D. Armstrong, N.A. Azad, E.M. Jaffee, E.T. Roussos Torres

Acquisition of data (provided animals, acquired and managed patients, provided facilities, etc.): B.J. Christmas, C.I. Rafie, B.A. Scott, H.S. Ma, K.A. Cruz, E.T. Roussos Torres

Analysis and interpretation of data (e.g., statistical analysis, biostatistics, computational analysis): B.J. Christmas, C.I. Rafie, A.C. Hopkins, H.S. Ma, N.A. Azad, E.M. Jaffee, E.T. Roussos Torres

Writing, review, and/or revision of the manuscript: B.J. Christmas, C.I. Rafie, H.S. Ma, T.D. Armstrong, R.M. Connolly, N.A. Azad, E.M. Jaffee, E.T. Roussos Torres

Administrative, technical, or material support (i.e., reporting or organizing data, constructing databases): B.J. Christmas, C.I. Rafie, N.A. Azad, E.T. Roussos Torres

Study supervision: T.D. Armstrong, N.A. Azad, E.T. Roussos Torres
Other (provided hands-on help with the tissue processing of many samples for the purpose of data collection; also ordered many of the reagents and supplies needed): S. Woolman
Other (provided regular input along course of study regarding treatment of breast cancer, clinical relevance): R.M. Connolly

Acknowledgments

E.M. Jaffee's lab members are supported through NIH RO1CA184926; Stand Up 2 Cancer–Lustgarten Foundation Pancreatic Cancer Convergence Dream Team Translational Research Grant (Grant Number: SU2C-AACR-DT14-14) and Stand Up To Cancer, which is a program of the Entertainment Industry Foundation administered by the American Association for Cancer Research; a gastrointestinal cancers Spore grant—NIH/NCI P50CA062924; and the Lustgarten Foundation's Research Investigator's Award Program. E.M. Jaffee and E.T. Roussos Torres also acknowledge funding from the Broccoli Foundation, The Bloomberg~Kimmel Institute for Cancer Immunotherapy, The Skip Viragh Center for Pancreas Cancer Clinical Research and Patient Care, and The Commonwealth Foundation for Cancer Research. E.T. Roussos Torres is funded through the MacMillan Pathway to Independence Fellowship as well as the Training Grant (5T32 CA009071-34) "Molecular Targets for Cancer Detection and Treatment."

We would like to thank all members of the Jaffee lab for help throughout the course of these experiments. We would like to thank Sudipto Ganguly from Dr. Drew Pardoll's lab for his guidance using NanoString technology. We thank Dr. Elana Fertig for her input regarding revisions and her thorough review of the manuscript. Additionally, we would like to thank Syndax Pharmaceuticals for supplying the entinostat used in these experiments. We would also like to thank Michael Palien for his expert artistic skills used to create the image in Fig. 7.

The costs of publication of this article were defrayed in part by the payment of page charges. This article must therefore be hereby marked *advertisement* in accordance with 18 U.S.C. Section 1734 solely to indicate this fact.

Received February 7, 2018; revised June 8, 2018; accepted October 18, 2018; published first October 19, 2018.

References

1. Denkert C, von Minckwitz G, Darb-Esfahani S, Lederer B, Heppner BI, Weber KE, et al. Tumour-infiltrating lymphocytes and prognosis in different subtypes of breast cancer: a pooled analysis of 3771 patients treated with neoadjuvant therapy. Lancet Oncol 2018;19: 40–50.
2. Solinas C, Gombos A, Latifyan S, Piccart-Gebhart M, Kok M, Buisseret L. Targeting immune checkpoints in breast cancer: an update of early results. ESMO Open 2017;2:e000255.
3. Nanda R, Chow LQM, Dees EC, Berger R, Gupta S, Geva R, et al. Pembrolizumab in patients with advanced triple-negative breast cancer: Phase Ib KEYNOTE-012 Study. J Clin Oncol 2016;34:2460–7.
4. Dirix LY, Takacs I, Jerusalem G, Nikolinakos P, Arkenau H-T, Forero-Torres A, et al. Avelumab, an anti-PD-L1 antibody, in patients with locally advanced or metastatic breast cancer: a phase 1b JAVELIN Solid Tumor study. Breast Cancer Res Treat 2018;167:671–86.
5. Schmid P, Cruz C BF. Atezolizumab in metastatic TNBC (mTNBC): Long-term clinical outcomes and biomarker analyses. 2017 AACR Annual Meeting. Abstract #2986; 2017.
6. Rugo HS, Delord J-P, Im SA, Ott PA, Piha-Paul SA, Bedard PL, et al. Preliminary efficacy and safety of pembrolizumab (MK-3475) in patients with PD-L1-positive, estrogen receptor-positive (ER+)/HER2 negative advanced breast cancer enrolled in KEYNOTE-028. 2015 San Antonio Breast Cancer Symposium. Abstract S5-07; 2015.
7. Tolaney S, Savulsky C, Aktan G, Xing D, Almonte A, Karantza V, et al. Abstract P5-15-02: Phase 1b/2 study to evaluate eribulin mesylate in combination with pembrolizumab in patients with metastatic triple-negative breast cancer. Cancer Res 2017;77:P5-15-02-P5-15-02.
8. Adams S, Schmid P, Rugo HS, Winer EP, Loirat D, Awada A, et al. Phase 2 study of pembrolizumab (pembro) monotherapy for previously treated metastatic triple-negative breast cancer (mTNBC): KEYNOTE-086 cohort A. J Clin Oncol 2017;35, no. 15_suppl (May 2017) 1008–1008.
9. Adams S, Loi S, Toppmeyer D, Cescon DW, De Laurentiis M, Nanda R, et al. Phase 2 study of pembrolizumab as first-line therapy for PD-L1–positive metastatic triple-negative breast cancer (mTNBC): Preliminary data from KEYNOTE-086 cohort B. J Clin Oncol May 2017;35, no. 15_suppl (May 2017) 1088–1088.
10. SABCS 2017: Combination of pembrolizumab and trastuzumab shows early promise for patients with trastuzumab-resistant breast cancer. The ASCO Post [cited 2018 Feb 2].
11. Kim K, Skora AD, Li Z, Liu Q, Tam AJ, Blosser RL, et al. Eradication of metastatic mouse cancers resistant to immune checkpoint blockade by suppression of myeloid-derived cells. Proc Natl Acad Sci USA 2014; 111:11774–9.
12. Stagg J, Loi S, Divisekera U, Ngiow SF, Duret H, Yagita H, et al. Anti-ErbB-2 mAb therapy requires type I and II interferons and synergizes with anti-PD-1 or anti-CD137 mAb therapy. Proc Natl Acad Sci USA 2011;108: 7142–7.
13. Brahmer JR, Tykodi SS, Chow LQM, Hwu W-J, Topalian SL, Hwu P, et al. Safety and activity of anti–PD-L1 antibody in patients with advanced cancer. N Engl J Med 2012;366:2455–65.
14. Royal RE, Levy C, Turner K, Mathur A, Hughes M, Kammula US, et al. Phase 2 trial of single agent Ipilimumab (anti-CTLA-4) for locally advanced or metastatic pancreatic adenocarcinoma. J Immunother 2010;33:828–33.
15. Lutz ER, Wu AA, Bigelow E, Sharma R, Mo G, Soares K, et al. Immunotherapy converts nonimmunogenic pancreatic tumors into immunogenic foci of immune regulation. Cancer Immunol Res 2014;2:616–31.
16. Bronte V, Serafini P, Mazzoni A, Segal DM, Zanovello P. L-arginine metabolism in myeloid cells controls T-lymphocyte functions. Trends Immunol 2003;24:302–6.
17. Kusmartsev S, Nagaraj S, Gabrilovich DI. Tumor-associated CD8+ T cell tolerance induced by bone marrow-derived immature myeloid cells. J Immunol 2005;175:4583–92.
18. Kamran N, Kadiyala P, Saxena M, Candolfi M, Li Y, Moreno-Ayala MA, et al. Immunosuppressive myeloid cells' blockade in the glioma microenvironment enhances the efficacy of immune-stimulatory gene therapy. Mol Ther 2017;25:232–48.
19. Yang R, Cai Z, Zhang Y, Yutzy WH th, Roby KF, Roden RB. CD80 in immune suppression by mouse ovarian carcinoma-associated Gr-1+CD11b+ myeloid cells. Cancer Res 2006;66:6807–15.
20. Marvel D, Gabrilovich DI. Myeloid-derived suppressor cells in the tumor microenvironment: expect the unexpected. J Clin Invest 2015; 125:3356–64.
21. Orillion A, Hashimoto A, Damayanti N, Shen L, Adelaiye-Ogala R, Arisa S, et al. Entinostat neutralizes myeloid-derived suppressor cells and enhances the antitumor effect of PD-1 inhibition in murine models of lung and renal cell carcinoma. Clin Cancer Res 2017;23:5187–201.
22. Tomita Y, Lee M-J, Lee S, Tomita S, Chumsri S, Cruickshank S, et al. The interplay of epigenetic therapy and immunity in locally recurrent or metastatic estrogen receptor-positive breast cancer: Correlative analysis of ENCORE 301, a randomized, placebo-controlled phase II trial of exemestane with or without entinostat. Oncoimmunology 2016;5:e1219008.
23. Weiss VL, Lee TH, Song H, Kouo TS, Black CM, Sgouros G, et al. Trafficking of high avidity HER-2/neu-specific T cells into HER-2/neu-expressing tumors after depletion of effector/memory-like regulatory T cells. PLoS One 2012;7:e31962.
24. Reilly RT, Gottlieb MB, Ercolini AM, Machiels JP, Kane CE, Okoye FI, et al. HER-2/neu is a tumor rejection target in tolerized HER-2/neu transgenic mice. Cancer Res 2000;60:3569–76.
25. Mace K, Mayhew E, Mihich E, Ehrke MJ, Lei RY, Weintraub D, et al. Alterations in murine host defense functions by adriamycin or liposome-encapsulated adriamycin. Cancer Res 1988;48:130–6.

26. Corbett TH, Roberts BJ, Leopold WR, Peckham JC, Wilkoff LJ, Griswold DP, et al. Induction and chemotherapeutic response of two transplantable ductal adenocarcinomas of the pancreas in C57BL/6 mice. Cancer Res 1984;44:717–26.
27. Leao IC, Ganesan P, Armstrong TD, Jaffee EM. Effective depletion of regulatory T cells allows the recruitment of mesothelin-specific CD8 T cells to the antitumor immune response against a mesothelin-expressing mouse pancreatic adenocarcinoma. Clin Transl Sci 2008;1:228–39.
28. Ercolini AM, Machiels J-PH, Chen YC, Slansky JE, Giedlen M, Reilly RT, et al. Identification and characterization of the immunodominant rat HER-2/neu MHC class I epitope presented by spontaneous mammary tumors from HER-2/neu-transgenic mice. J Immunol 2003;170: 4273–80.
29. Soares KC, Foley K, Olino K, Leubner A, Mayo SC, Jain A, et al. A preclinical murine model of hepatic metastases. J Vis Exp 2014;27:51677.
30. Lee JW, Komar CA, Bengsch F, Graham K, Beatty GL. Genetically engineered mouse models of pancreatic cancer: The KPC Model (*LSL-Kras* $^{G12D/+}$;*LSL-Trp53* $^{R172H/+}$;*Pdx-1-Cre*), its variants, and their application in immuno-oncology drug discovery. Curr Protoc Pharmacol 2016;73:14.39.1–14.39.20.
31. Foote JB, Kok M, Leatherman JM, Armstrong TD, Marcinkowski BC, Ojalvo LS, et al. A STING agonist given with OX40 receptor and PD-L1 modulators primes immunity and reduces tumor growth in tolerized mice. Cancer Immunol Res 2017;5:468–79.
32. Mueller S, Engleitner T, Maresch R, Zukowska M, Lange S, Kaltenbacher T, et al. Evolutionary routes and KRAS dosage define pancreatic cancer phenotypes. Nature 2018;554:62–8.
33. Hingorani SR, Wang L, Multani AS, Combs C, Deramaudt TB, Hruban RH, et al. Trp53R172H and KrasG12D cooperate to promote chromosomal instability and widely metastatic pancreatic ductal adenocarcinoma in mice. Cancer Cell 2005;7:469–83.
34. Pardoll DM. The blockade of immune checkpoints in cancer immunotherapy. Nat Rev Cancer 2012;12:252–64.
35. Soares KC, Rucki AA, Wu AA, Olino K, Xiao Q, Chai Y, et al. PD-1/PD-L1 blockade together with vaccine therapy facilitates effector T cell infiltration into pancreatic tumors. J Immunother 2015;38:1–11.
36. Shakespear MR, Halili MA, Irvine KM, Fairlie DP, Sweet MJ. Histone deacetylases as regulators of inflammation and immunity. Trends Immunol 2011;32:335–43.
37. Klampfer L, Huang J, Swaby L-A, Augenlicht L. Requirement of histone deacetylase activity for signaling by STAT1. J Biol Chem 2004;279: 30358–68.
38. Zhang Q, Zhao K, Shen Q, Han Y, Gu Y, Li X, et al. Tet2 is required to resolve inflammation by recruiting Hdac2 to specifically repress IL-6. Nature 2015;525:389–93.
39. Pan W, Zhu S, Qu K, Meeth K, Cheng J, He K, et al. The DNA methylcytosine dioxygenase Tet2 sustains immunosuppressive function of tumor-infiltrating myeloid cells to promote melanoma progression. Immunity 2017;47: 284–297.e5.
40. Ritchie ME, Phipson B, Wu D, Hu Y, Law CW, Shi W, et al. limma powers differential expression analyses for RNA-sequencing and microarray studies. Nucleic Acids Res 2015;43:e47.
41. Luo W, Friedman MS, Shedden K, Hankenson KD, Woolf PJ. GAGE: generally applicable gene set enrichment for pathway analysis. BMC Bioinformatics 2009;10:161.
42. Luo W, Brouwer C. Pathview: an R/Bioconductor package for pathway-based data integration and visualization. Bioinformatics 2013;29: 1830–1.
43. Garon EB, Rizvi NA, Hui R, Leighl N, Balmanoukian AS, Eder JP, et al. Pembrolizumab for the treatment of non–small-cell lung cancer. N Engl J Med 2015;372:2018–28.
44. Thompson RH, Kuntz SM, Leibovich BC, Dong H, Lohse CM, Webster WS, et al. Tumor B7-H1 is associated with poor prognosis in renal cell carcinoma patients with long-term follow-up. Cancer Res 2006;66:3381–5.
45. Shen L, Ciesielski M, Ramakrishnan S, Miles KM, Ellis L, Sotomayor P, et al. Class I histone deacetylase inhibitor entinostat suppresses regulatory T cells and enhances immunotherapies in renal and prostate cancer models. PLoS One 2012;7:e30815.
46. Slamon DJ, Leyland-Jones B, Shak S, Fuchs H, Paton V, Bajamonde A, et al. Use of chemotherapy plus a monoclonal antibody against HER2 for metastatic breast cancer that overexpresses HER2. N Engl J Med 2001;344:783–92.
47. Falkenberg KJ, Johnstone RW. Histone deacetylases and their inhibitors in cancer, neurological diseases and immune disorders. Nat Rev Drug Discov 2014;13:673–91.
48. Baitsch L, Legat A, Barba L, Fuertes Marraco SA, Rivals J-P, Baumgaertner P, et al. Extended co-expression of inhibitory receptors by human CD8 T-cells depending on differentiation, antigen-specificity and anatomical localization. PLoS One 2012;7:e30852.
49. Blackburn SD, Shin H, Haining WN, Zou T, Workman CJ, Polley A, et al. Coregulation of $CD8^+$ T cell exhaustion by multiple inhibitory receptors during chronic viral infection. Nat Immunol 2009; 10:29–37.
50. Shimizu K, Iyoda T, Okada M, Yamasaki S, Fujii S. Immune suppression and reversal of the suppressive tumor microenvironment. Int Immunol 2018;30:445–55.
51. Pan P-Y, Ma G, Weber KJ, Ozao-Choy J, Wang G, Yin B, et al. Immune stimulatory receptor CD40 is required for T-cell suppression and T regulatory cell activation mediated by myeloid-derived suppressor cells in cancer. Cancer Res 2010;70:99–108.
52. Horikawa N, Abiko K, Matsumura N, Hamanishi J, Baba T, Yamaguchi K, et al. Expression of vascular endothelial growth factor in ovarian cancer inhibits tumor immunity through the accumulation of myeloid-derived suppressor cells. Clin Cancer Res 2017;23:587–99.
53. Wei J, Besner GE. M1 to M2 macrophage polarization in heparin-binding epidermal growth factor-like growth factor therapy for necrotizing enterocolitis. J Surg Res 2015;197:126–38.
54. Kaneda MM, Messer KS, Ralainirina N, Li H, Leem CJ, Gorjestani S, et al. Erratum: Corrigendum: PI3Kγ is a molecular switch that controls immune suppression. Nature 2017;542:124.
55. Wu T, Zhao Y, Wang H, Li Y, Shao L, Wang R, et al. mTOR masters monocytic myeloid-derived suppressor cells in mice with allografts or tumors. Sci Rep 2016;6:20250.
56. Hardbower DM, Singh K, Asim M, Verriere TG, Olivares-Villagómez D, Barry DP, et al. EGFR regulates macrophage activation and function in bacterial infection. J Clin Invest 2016;126:3296–312.
57. Vasquez-Dunddel D, Pan F, Zeng Q, Gorbounov M, Albesiano E, Fu J, et al. STAT3 regulates arginase-I in myeloid-derived suppressor cells from cancer patients. J Clin Invest 2013;123:1580–9.
58. Kumar V, Donthireddy L, Marvel D, Condamine T, Wang F, Lavilla-Alonso S, et al. Cancer-associated fibroblasts neutralize the anti-tumor effect of CSF1 receptor blockade by inducing PMN-MDSC infiltration of tumors. Cancer Cell 2017;32:654–668.e5.
59. Condamine T, Gabrilovich DI. Molecular mechanisms regulating myeloid-derived suppressor cell differentiation and function. Trends Immunol 2011;32:19–25.
60. Dodd KM, Yang J, Shen MH, Sampson JR, Tee AR. mTORC1 drives HIF-1α and VEGF-A signalling via multiple mechanisms involving 4E-BP1, S6K1 and STAT3. Oncogene 2015;34:2239–50.
61. Wei D, Le X, Zheng L, Wang L, Frey JA, Gao AC, et al. Stat3 activation regulates the expression of vascular endothelial growth factor and human pancreatic cancer angiogenesis and metastasis. Oncogene 2003;22: 319–29.
62. Niu G, Wright KL, Huang M, Song L, Haura E, Turkson J, et al. Constitutive Stat3 activity up-regulates VEGF expression and tumor angiogenesis. Oncogene 2002;21:2000–8.
63. Wei L-H, Kuo M-L, Chen C-A, Chou C-H, Lai K-B, Lee C-N, et al. Interleukin-6 promotes cervical tumor growth by VEGF-dependent angiogenesis via a STAT3 pathway. Oncogene 2003;22:1517–27.
64. Brocks D, Schmidt CR, Daskalakis M, Jang HS, Shah NM, Li D, et al. DNMT and HDAC inhibitors induce cryptic transcription start sites encoded in long terminal repeats. Nat Genet 2017;49:1052–60.